

1 **Crossing hydrological and geochemical modeling to understand the spatiotemporal variability**
2 **of water chemistry in a headwater watershed (Strengbach, France)**

3 Julien Ackerer*, Benjamin Jeannot, Frederick Delay, Sylvain Weill, Yann Lucas, Bertrand Fritz,
4 Daniel Viville, François Chabaux

5 Laboratoire d'Hydrologie et de Géochimie de Strasbourg, Université de Strasbourg, CNRS,
6 ENGEES, 1 rue Blessig, 67084 Strasbourg Cedex, France

7

8

9 Corresponding authors : Julien Ackerer, Benjamin Jeannot, Frederick Delay (fdelay@unistra.fr),
10 François Chabaux (fchabaux@unistra.fr).

11

12

13

14

15

16

17

18

19

20 **Abstract**

21 Understanding the variability of the chemical composition of surface waters is a major issue for
22 the scientific community. To date, the study of concentration-discharge relations has been
23 intensively used to assess the spatiotemporal variability of the water chemistry at watershed
24 scales. However, the lack of independent estimations of the water transit times within
25 catchments limits the ability to model and predict the water chemistry with only geochemical
26 approaches. In this study, a dimensionally reduced hydrological model coupling surface flow
27 with subsurface flow (i.e., the Normally Integrated Hydrological Model, NIHM) has been used to
28 constrain the distribution of the flow lines in a headwater catchment (Strengbach watershed,
29 France). Then, hydrogeochemical simulations with the code KIRMAT (i.e., Kinetic Reaction and
30 MAss Transport) are performed to calculate the evolution of the water chemistry along the flow
31 lines. Concentrations of dissolved silica (H_4SiO_4) and in basic cations (Na^+ , K^+ , Mg^{2+} , and Ca^{2+}) in
32 the spring and piezometer waters are correctly reproduced with a simple integration along the
33 flow lines. The seasonal variability of hydraulic conductivities along the slopes is a key process to
34 understand the dynamic of flow lines and the changes of water transit times in the watershed.
35 The covariation between flow velocities and active lengths of flow lines over changing
36 hydrological conditions reduces the variability of water transit times and explains why transit
37 times span much narrower variation ranges than the water discharges. These findings
38 demonstrate that the general chemostatic behavior of the water chemistry is a direct
39 consequence of the strong hydrological control of the water transit times within the catchment.
40 Our results also show that a better knowledge of the concentration-mean transit time relations
41 (C-MTT relations) is an interesting new step to understand the diversity of C-Q shapes for

42 chemical elements. The good matching between the measured and modeled concentrations
43 while respecting the water-rock times provided by the hydrological simulations also shows that
44 it is possible to capture the chemical composition of waters using simply determined reactive
45 surfaces and experimental kinetic constants. The results of our simulations also strengthen the
46 idea that the low surfaces calculated from the geometrical shapes of primary minerals are a
47 good estimate of the reactive surfaces within the natural environment.

48

49 **1- Introduction**

50 Understanding the effects of the ongoing climatic changes on the environment is a major issue
51 for the coming years. The global increase of temperature is expected to affect the hydrological
52 cycle at a large scale, and providing a precise estimation of its repercussion on the evolution of
53 soils and on the chemistry of waters remains challenging. This challenge results from the wide
54 diversity of hydrological, geochemical, and biological processes, and of their coupling, that
55 operate at the Earth's surface (e.g., Gislason et al., 2009; Godd ris et al., 2013; Beaulieu et al.,
56 2012; 2016). Up today, the study of concentration-discharge relations (C-Q relations) has been
57 intensively used to assess the coupling between hydrological and geochemical processes at the
58 hillslope or watershed scales (Godsey et al., 2009; Kim et al., 2017; Ameli et al., 2017; Diamond
59 and Cohen, 2018).

60 C-Q relations are acknowledged to integrate critical zone structure, the hydrological dynamics
61 and the geochemical processes of watersheds (Chorover et al., 2017). Recent studies debated to
62 which extend the chemical variability of waters is explained by a mixing of different water
63 sources (Zhi et al., 2019), the chemical contrasts between deep and shallow waters (Kim et al.,
64 2017), the variability of transit times (Ackerer et al., 2018) and/or seasonally variable flow paths
65 (Herndon et al., 2018). It is clear that a good knowledge of the water flow paths and of their
66 seasonal variability is an important new step to better constrain the water transit times within
67 catchments, and then, to correctly understand the temporal fluctuations of the composition of
68 waters. Modeling such variability of water flow paths and water geochemical composition
69 would require further development of modeling approaches able to combine hydrological and
70 geochemical processes (e.g. Steefel et al., 2005; Kirchner, 2006).

71 Recent efforts in hydrological modeling were conducted to develop spatially distributed
72 approaches that better consider the interplay between surface and subsurface processes (e.g.,
73 Gunduz and Aral, 2005; Kampf and Burges, 2007; Camporese et al., 2010). Due to the
74 complexity of flows in the hydrological processes, many modeling approaches are based on the
75 full resolution of Richard's and Saint Venant equations to correctly describe the interactions
76 between stream, overland and subsurface waters (Kampf and Burges, 2007). These approaches
77 have shown their ability to capture the hydrological functioning of various watersheds, knowing
78 that the full resolution of Richard's and Saint Venant equations requires long computational
79 times and faces calibration and parameterization difficulties (Ebel and Loague, 2006; Mirus et
80 al., 2011). Questions have been raised regarding the optimal complexity of the equations that
81 are needed to correctly treat the hydrology of catchments in their surface and subsurface
82 compartments with reasonable computation times (Gunduz and Aral, 2005).

83 Low-dimensional models have attracted growing interest because they represent an interesting
84 compromise between equation complexity, computational time, and result accuracy (Pan et al.,
85 2015; Hazenberg et al., 2016; Weill et al., 2013; 2017; Jeannot et al., 2018). The reduction of
86 dimensionality is mainly associated with a subsurface compartment (including both the vadose
87 and the saturated zones) modeled as a two-dimensional layer. Flow and transport processes are
88 integrated over a vertical direction or a direction normal to bedrock and manipulate averaged
89 (integrated) hydrodynamic properties. These low-dimensional models recently demonstrated
90 their ability to reproduce the results from fully dimensioned approaches in small catchments
91 while reducing computational costs (Pan et al., 2015; Jeannot et al., 2018). Nonetheless, the
92 water transit times calculated from these depth-integrated models are rarely confronted with

93 the water-rock interaction times inferred from hydrogeochemical modeling of water chemistry
94 in watersheds.

95 For its part, the understanding of the hydrogeochemical functioning of the critical zone has
96 been significantly advanced by the implementation of reactive-transport laws in geochemical
97 modeling codes (Steeffel et al., 2005; Lucas et al., 2010; 2017; Godd ris et al., 2013; Li et al.,
98 2017). These developments allow for considering a variety of processes, such as flow and
99 transport processes, ion exchanges, biogeochemical reactions, and the interplay between
100 primary mineral dissolution and secondary mineral precipitation (Moore et al., 2012; Lebedeva
101 and Brantley, 2013; Ackerer et al., 2018). Reactive transport models have been used to explore
102 a wide variety of scientific issues, including the study of global atmospheric CO₂ consumption by
103 weathering reactions (Godd ris et al., 2013; Li et al., 2014), the formation and evolution of soil
104 and regolith profiles (Maher et al., 2009; Navarre-Sitchler et al., 2009; Lebedeva and Brantley,
105 2013), and the variability of water quality and chemistry in the environment (Lucas et al., 2010;
106 2017; Ackerer et al., 2018). However, these approaches usually rely on a simple 1D flow path
107 through a regolith column or along a hill slope to model flow in the system (e.g. Maher, 2011;
108 Moore et al., 2012; Lucas et al., 2017; Ackerer et al., 2018). 1D reactive-transport models are
109 useful to discuss the key processes involved in the regolith formation and in the acquisition of
110 the water chemical composition, but these models cannot consider the complexity of the flow
111 trajectories in watersheds, and hence, its effects on the water chemistry.

112 A new step is therefore necessary for the development of hydrogeochemical modeling
113 approaches that are applicable at the watershed scale and are able to integrate the complexity
114 of the water flows and the diversity of the water-rock interaction processes. Recent efforts have

115 been undertaken in the direction of merging hydrological and geochemical codes, with for
116 example, the parallel reactive transport code ParCrunchFlow (Beisman et al., 2015), or the
117 coupled hydrogeochemical code RT-Flux-PIHM (Bao et al., 2017; Li et al., 2017). As an
118 alternative to fully dimensioned codes, this work proposes an original low-dimensional
119 approach, with relatively short computation times and applicable at the watershed scale. This
120 study is combining for the first time in this manner the results from a hydrological low-
121 dimensional (depth-integrated for the subsurface) but spatially distributed model (NIHM) with a
122 reactive-transport model (KIRMAT). The combination allows for simulating over time and space
123 the flow trajectories, the flow rates, the weathering reactions, and the evolution of the water
124 chemistry within a headwater watershed, the Strengbach catchment.

125 This catchment is one of the reference observatories of the French critical zone network
126 (OZCAR), where multidisciplinary studies, including hydrological, geochemical and geological
127 investigations, have been performed since 1986 (“Observatoire Hydrogéo chimique de
128 l’Environnement”, OHGE; <http://ohge.unistra.fr>; El Gh’Mari, 1995; Fichter et al., 1998; Viville et
129 al., 2012; Gangloff et al., 2014; 2016; Prunier et al., 2015; Pan et al., 2015; Ackerer et al., 2016;
130 2018; Beaulieu et al., 2016; Chabaux et al., 2017; 2019; Schmitt et al., 2017; 2018; Daval et al.,
131 2018; see also Pierret et al., 2018 for an updated overview of the Strengbach watershed).

132 **2- Site presentation and data acquisition**

133 The Strengbach catchment is a small watershed (0.8 km²) located in the Vosges Mountains of
134 northeastern France at altitudes between 883 and 1147 m. Its hydroclimatic characteristics can
135 be found in Viville et al. (2012) or in Pierret et al. (2018). It is marked by a mountainous oceanic

136 climate, with an annual mean temperature of 6 °C and an annual mean rainfall of approximately
137 1400 mm, with 15 to 20% falling as snow during two to four months per year. The snow cover
138 period is quite variable from year to year, and may not be continuous over the entire winter.
139 The annual mean evapotranspiration is of approximately 600 mm, and the annual mean runoff
140 of approximately 800 mm (Viville et al., 2012). The watershed is currently covered by a beech
141 and spruce forest. The bedrock is a base-poor Hercynian granite covered by a 50 to 100 cm-thick
142 acidic and coarse-in-texture soil. The granitic bedrock was fractured and hydrothermally altered,
143 with a stronger degree of hydrothermal overprinting in the northern than the southern part of
144 the catchment (Fichter et al., 1998). The granite was also affected by surface weathering
145 processes during the Quaternary (Ackerer et al., 2016). The porous and uppermost part of the
146 granitic basement constitutes an aquifer from 2 to approximately 8 meters thickness. In the
147 Strengbach watershed, the major floods and high-flow events usually occur during snowmelt
148 periods at the end of the winter season or in the early spring. In contrast, the low-flow periods
149 commonly happen at the end of the summer or during the autumn. Several springs naturally
150 emerge along the slopes (figure 1). The watershed has been equipped with several piezometers
151 and boreholes since 2012, those being located along the slopes on both sides of the watershed
152 (figure 1 in Chabaux et al., 2017).

153 Spring waters have been regularly collected and analyzed since 2005, with monthly sampling
154 supplemented by a few specific campaigns to cover the complete range of water discharges in
155 the watershed. Piezometer waters have been collected only during specific sampling campaigns
156 over the period 2012-2015, and as for the spring waters, these sampling campaigns cover
157 different hydrological conditions from wet to dry periods. The soil solutions were collected with

158 a monthly frequency on the southern slope at a beech site (named HP) and to the north at a
159 spruce site (named VP; figure 1; more details in Prunier et al., 2015 or Chabaux et al., 2019). For
160 all the collected waters, the concentrations of the major dissolved species and the pH were
161 determined by following the analytical techniques used at LHyGeS (Strasbourg, France) and
162 detailed in Gangloff et al. (2014) and Prunier et al. (2015). Discharges of water from the springs
163 were measured during the sampling campaigns, as were the water levels within the
164 piezometers.

165 The mineralogy and the porosity of the bedrock have been studied in detail in previous studies
166 (El Gh'Mari, 1995; Fichter et al., 1998). On the southern part of the catchment, the weakly
167 hydrothermally altered granite (named HPT, figure 1) is mainly composed of quartz (35%), albite
168 (31%), K-feldspar (22%) and biotite (6%). It also contains small amounts of muscovite (3%),
169 anorthite (2%), apatite (0.5%) and clay minerals (0.5%). On the northern part of the catchment,
170 the lithology is more variable, with the presence of gneiss close to the crest lines and the
171 occurrence of hydrothermally altered granite on the rest of the slopes (El Gh'Mari, 1995, figure
172 1).

173 The hydrological, geochemical and petrological data obtained from these field investigations are
174 the basis of the modeling exercise presented in this study. More precisely, this study is based on
175 hydrogeochemical data from 2005 to 2015 for waters from four springs of the southern part
176 (CS1, CS2, CS3 and CS4) and one spring of the northern part (RH3) of the watershed.
177 Hydrogeochemical data obtained over the period 2012-2015 for two piezometers (PZ3, PZ5) of
178 the southern part of the watershed are also studied. The overall hydrogeochemical database is

179 available as supplementary tables (tables EA1 to EA9). The specific chemical data from spring
180 and piezometer waters modeled in this study are reported in table 1.

181 **3- Modeling methods**

182 The modeling developments presented in this study represent a new step in the efforts
183 undertaken to constrain the mechanisms controlling the geochemical composition of surface
184 waters and to understand their spatial and temporal variations at the scale of headwater
185 mountainous watersheds (Schaffhauser et al., 2014; Lucas et al., 2017; Ackerer et al., 2018). The
186 main innovation of this present work is to couple a spatially distributed and low-dimensional
187 hydrological model with a reactive transport code to constrain the spatiotemporal variability of
188 chemical composition of waters from a headwater watershed. To the best of our knowledge,
189 this is the first time that such a coupling between low-dimensional hydrological and
190 hydrogeochemical modeling approaches has been attempted in this way at the watershed scale.

191 **3-1 Hydrological modeling**

192 To assess the water flows in the watershed, several simulations were performed with the
193 hydrological code NIHM (Normally Integrated Hydrological Model; Pan et al., 2015; Weill et al.,
194 2017; Jeannot et al., 2018). This code is a coupled stream, overland, and low-dimensional
195 (depth-integrated) subsurface flow model developed at LHyGeS and already tested in the
196 Strengbach watershed (Pan et al., 2015). The stream and overland flows are described by a
197 diffusive-wave equation, and the subsurface flow is handled through an integration (in a
198 direction normal to bedrock) of the unsaturated-saturated flow equation from the bedrock to
199 the soil surface (Weill et al., 2017). The exchanges of water between the surface and subsurface

200 flows are addressed via the hydraulic head differences between the compartments (Jeannot et
201 al., 2018).

202 Regarding the hydrological simulations, the parameters of the aquifer have been adjusted in
203 NIHM through a calibration-validation process. Several zones of heterogeneity were defined
204 based on field observations (Ackerer et al., 2016; Chabaux et al., 2017). In each of these zones,
205 the saturated hydraulic conductivity, the depth of substratum, and the porosity, were set to
206 uniform values. Other parameters were set to uniform values over the whole catchment (see
207 table 2). The thickness of the aquifer that was used for the simulations varied from 2 meters
208 near the main crests to up to 8 meters in the middle of the watershed (figure 2), in agreement
209 with the data obtained during the recent geological investigations and drilling campaigns
210 undertaken at the catchment (Ackerer et al., 2016; Chabaux et al., 2017). The uniform
211 precipitations over space applied at the surface of the catchment are drawn from data of the
212 pluviometric station located at the highest elevation of the watershed (site PA, figure 1). The
213 hydrological model NIHM was then run over a first time period (years 1996-1997). By a process
214 of trial and error, the parameters were gradually modified to improve the fitting between the
215 observed and simulated flow rates at the outlet of the catchment (table 2). The fit was
216 quantified by the root mean square error (RMSE) and the Kling-Gupta efficiency coefficient
217 (KGE; Gupta et al., 2009).

218 Once the best fit was obtained, the model was then run over another time period (2010-2015),
219 but without changing the parameters anymore, and the quality of the fit was re-assessed for
220 this new time-period with the KGE and RMSE. Figure 2 shows the result for the 2010-2015 time
221 period. Once the water discharges were correctly reproduced at the outlet, a backtracking

222 approach was used to constrain the origin of subsurface water exiting the system at prescribed
223 locations, and the spatiotemporal variability of the flow lines within the watershed. To back
224 track the water particles, the velocity fields calculated by the NIHM model were inverted in their
225 direction, and the locations of the backtracked particles were saved at each time-step. A daily
226 time-step was used for the backtracking, as a compromise between computational efforts and a
227 refined description of the transient velocity fields. A schematic representation of the
228 backtracking approach is given in figure 3. This methodology allows for constraining the flow
229 lines that bring waters for a given time and at a given position on the catchment. This
230 information is of major interest to determine the origin of the spring and piezometer waters. It
231 is shown at the catchment scale, that flows are mainly driven by gravity in association with the
232 steep slopes of the watershed, the latter being almost evenly drained over its whole surface
233 area (figure 4). For each water sampling area, ten flow lines that bring water to the location of
234 interest were determined (figure 4), together with a few features of the flow lines, including:
235 local velocities, mean velocities, and length of the flow paths.

236 It is worth noting that NIHM is a depth-integrated model for its subsurface compartment where
237 flow is simulated over a 2D-mesh and under the assumption of an instantaneous hydrostatic
238 equilibrium in the direction perpendicular to the substratum. Therefore, times calculated along
239 the backtracked streamlines correspond to a date, x days before arrival, at which a water
240 particle entered the subsurface or passed at a given location along the streamline. Streamlines
241 calculated via backtracking and reaching sampling sites only consider flow in the subsurface
242 compartment and are conditional to an arrival date at a prescribed location. As backtracked

243 streamlines are not associated with mean water flux values, the transit time distributions drawn
244 from streamline calculations are only an approximation of the actual transit time distributions.

245 **3-2 Hydrogeochemical modeling**

246 The simulations of the water chemical composition along the flow lines were performed with
247 the hydrogeochemical KIRMAT code (Kinetic of Reaction and MAAss Transport; Gérard et al.,
248 1998; Lucas et al., 2010; Ngo et al., 2014). KIRMAT is a thermokinetic model derived from the
249 Transition State Theory (TST, Eyring, 1935; Murphy and Helgeson, 1987) that simultaneously
250 solves the equations describing geochemical reactions and transport mass balance in a 1D-
251 porous medium. The mass transport includes the effects of one-dimensional convection,
252 diffusion and kinematic dispersion. Chemical reactions account for the dissolution of primary
253 minerals and oxido-reduction reactions, in addition to the formation of secondary minerals and
254 clay minerals. Thermodynamic and kinetic data for the primary minerals are available in
255 supplementary materials (tables EA10, EA11 and EA12).

256 The clay fraction is defined as a solid solution made up of a combination of pure clay end-
257 members. The clay end-members are defined on the basis of X-ray diffraction analyses of clay
258 minerals present in bedrock samples collected in the field (Fichter et al., 1998; Ackerer et al.,
259 2016; 2018). They consist of K-Illites, Mg-Illites, Ca-Illites, Montmorillonites, Na-
260 Montmorillonites, K-Montmorillonites, Ca-Montmorillonites and Mg-Montmorillonites
261 (supplementary material table EA13). During the hydrogeochemical simulations, the clay solid
262 solution is precipitated at thermodynamic equilibrium and its composition varies over time,
263 depending on the evolution of the water chemistry and the bedrock mineralogy (Ackerer et al.,

264 2018). This multicomponent solid solution reproduces the diversity of the clay minerals formed
265 during low-temperature water-rock interactions (Tardy and Fritz, 1981).

266 The KIRMAT code also includes feedback effects between mineral mass budgets, reactive
267 surfaces, and the evolution of bedrock porosity (Ngo et al., 2014). The reactive surfaces of the
268 primary minerals were calculated by assuming a simple spherical geometry for all the minerals,
269 and the mean size of the minerals was estimated from the observation of thin sections from
270 bedrock samples. During simulations, clay mineral precipitation and the evolution of the
271 reactive surfaces of primary minerals are tracked together with chemical processes and water
272 chemical composition. Given the short time scales reported by the hydrological simulations
273 (monthly timescale), changes in the reactive surfaces of primary minerals over the simulation
274 time were negligible. Precipitation of other secondary minerals such as carbonates, hematite or
275 amorphous silica was also tested, but these minerals were not formed given the saturation
276 states calculated in the geochemical modeling (supplementary table EA14). Secondary mineral
277 precipitation is therefore controlled by clay mineral formation. The KIRMAT code has already
278 been applied in geochemical modeling of alluvial groundwaters (Lucas et al., 2010) and surface
279 waters (Lucas et al., 2017; Ackerer et al., 2018).

280 For this study, the modeling strategy is adapted from Ackerer et al. (2018) to consider the new
281 transit time constrains provided by the hydrological code NIHM. To capture the chemical
282 composition of the spring and the piezometer waters, numerical simulations were performed
283 along the flow lines that were determined through the backtracking approach. A sketch of the
284 hydrogeochemical modeling strategy is provided in figure 5. For each flow line, several KIRMAT
285 simulations were performed with different starting positions along the active part of the line.

286 The starting positions represent the locations at which the soil solutions percolate through the
287 subsurface shallow aquifer. These variable starting positions are spaced with a constant
288 distance along the flow line. The deepest soil solutions collected to the south at the beech site
289 (HP) and to the north at the spruce site (VP) were considered representative of the soil solutions
290 for the southern and northern slopes of the catchment, respectively. The data of soil solution
291 chemistry used in this study are available in Prunier et al. (2015) and in supplementary tables
292 (tables EA6 and EA7). These soil solutions integrate the surface processes occurring before
293 water percolation into the bedrock. Because the soil solutions are injected into the aquifer, the
294 temporal variability of the soil solution chemistry and its impact on the water-rock interactions
295 along the flow paths are accounted for in the modeling approach.

296 Data related to the bedrock properties, such as the mineralogical compositions, the mineral
297 reactive surfaces and the thermodynamic and kinetic constants, are given in Ackerer et al.
298 (2018) and in supplementary tables (tables EA10 to EA14). Mineral phases are assumed
299 homogeneously distributed over the regolith layer. By following this strategy, the simulations
300 that consider soil solutions percolating at the upper part of the catchment reflect the chemical
301 evolution of waters with long path lengths and long transit times within the aquifer. By contrast,
302 shorter path lengths and shorter transit times are associated with the percolation of soil
303 solutions that occurs in the vicinity of the sampling locations (figure 5). Because the springs or
304 the piezometers collect waters from different origins and with contrasted transit times,
305 integration along each water flow line was performed. The aim of the integration is to
306 determine the mean chemical composition resulting from the mixing of the waters
307 characterized by variable transit times (figure 5). The integrated chemical composition of the

308 waters provided by a given flow line is calculated by taking the arithmetic mean of the solute
309 concentrations calculated by the succession of the KIRMAT simulations along the flow line
310 (figure 5). This arithmetic mean reflects a simple full mixing of uniform water fluxes irrespective
311 of their short or long transit times. In other words, the geochemical simulations are based on
312 the hypothesis of spatially homogenous water-rock interactions along the flow lines. The soil
313 solutions are assumed to percolate uniformly within the aquifer and are then conveyed along
314 the slopes by uniformly distributed mass of water until reaching the sampling locations.

315 **4- Hydrological modeling results**

316 **4-1 Spatial variability of the flow lines**

317 The results provided by the hydrological code NIHM show that to the first order, the Strengbach
318 catchment is well drained and that the topography exerts an important control on the flow line
319 distribution (figure 4). Along the hillsides presenting linear or slightly convex slopes, the water
320 flow lines show simple characteristics. The flow paths are nearly parallel, and the water
321 velocities are similar along the different flow lines on this type of hillside. The water velocities
322 tend to increase when moving downstream, with slower velocities near the main crests and
323 higher velocities on the steepest parts of the hillsides. The waters collected along this type of
324 hillside are therefore characterized by small variability of transit times. This is the case for the
325 CS1, CS3 and RH3 spring waters located on the southern and northern parts of the catchment
326 (figure 4). This is also the case for the piezometers PZ3 and PZ5 in the southern part of the
327 watershed (figure 4). For the samplings located on linear or slightly convex slopes (CS1, CS3,

328 RH3, PZ3 and PZ5), the characteristics of the different flow lines that feed each site are
329 therefore comparable for a given site and for a given date.

330 By contrast, in the vicinity of the valley and in the topographic depressions, the hydrological
331 modeling indicates that the flow line characteristics are more variable. Because flow lines
332 coming from different hill-sides can feed a topographic depression, mixing of different flow lines
333 with variable flow paths and contrasted water velocities can occur at these locations. The
334 waters collected in valleys or in topographic depressions are therefore characterized by a higher
335 variability of transit times. This is the case for the CS2 and CS4 springs, which are located in a
336 depression in the axe of the small valley and surrounded by slopes with various orientations and
337 a complex flow line distribution (figure 4). For these two springs, the characteristics of the
338 different flow lines can be different for a given date.

339 **4-2 Temporal variability of the flow lines**

340 Hydrological modeling under general transient conditions can render the evolution over time of
341 water flows in the watershed but also of other hydraulic variables or parameters. As an
342 example, after an important rainfall event (30/03/2010 in figure 6), snapshots of the average
343 hydraulic conductivity in the subsurface show increasing values with decreasing elevation in the
344 watershed. The same observation holds for hydraulic conductivity during drought periods (see
345 29/11/2011, in figure 6). Provided that the hydraulic head gradient is largely dominated by the
346 topography and therefore almost constant over time (figure 6), the water velocities are
347 increasing along the flow lines from crests to valleys, irrespective of the wet versus dry
348 hydrological periods.

349 For the CS1 spring, the mean flow velocities along the flow lines vary from approximately 1
350 m/day to 7 m/day between the severe drought of 29/11/2011 and the strong flood of
351 30/03/2010 (figures 7A and 7B). These events correspond to the annual minimum and
352 maximum flow rates at the outlet of the Strengbach watershed. For the same dates, the mean
353 velocities vary from 2 – 12 m/day, 1 – 4 m/day and 1 – 9 m/day for the springs CS2, CS3 and
354 CS4, respectively. The variations from drought to flood are very similar for the piezometer
355 waters, with velocities in the ranges 2 – 10 m/day and 2 – 12 m/day for the PZ3 and PZ5
356 piezometers, respectively. The RH3 spring located on a steeper part of the northern slopes
357 exhibits flow velocity variations from 5 to 20 m/day from dry to flood conditions.

358 In addition to the flow velocity variations, the hydrological simulations also reveal variability in
359 the lengths of the active parts of the flow lines. Such variability is triggered by the particular
360 seasonal variations of the hydraulic conductivities within the catchment. During periods of
361 drought, the simulations indicate a strong decrease of hydraulic conductivities close to the main
362 crests and much smaller variations at mid-slopes (figure 6). The crests rapidly dry out, whereas
363 the areas at mid-slopes still supply some water to the stream network. These contrasting
364 hydrological behaviors result from the differences in aquifer thickness and water storage
365 between the crests and the other parts of the catchment (figure 2). Thin aquifer, flow
366 divergence and absence of feeding areas prevent large water storage on the crests, in
367 opposition to mid-slope parts with much thicker aquifers and the presence of feeding areas
368 upstream. This particular pattern simulated for the hydraulic conductivities implies that the
369 active parts of the flow lines extend up the main crests during important floods, whereas they
370 are limited to mid-slopes after a long dry period.

371 The consequence of this hydrological functioning is to moderate the seasonal variations of the
372 transit times of waters, as the active lengths of flow lines vary simultaneously with water flow
373 rates. Calculations indicate that for the spring and piezometer waters collected in this study, the
374 mean transit times of waters only vary from approximately 1.75 to 4 months between the
375 strongest flood and the driest conditions. These short subsurface water transit times are
376 explained by the small size of the catchment and the relatively steep slopes.

377 **5- Hydrogeochemical modeling results**

378 **5-1 CS1 and CS3 springs (southern slope)**

379 The CS1 and CS3 springs emerge on the same slope and drain the same rocks. Their hydrological
380 behavior is also very similar in terms of flow lines and water transit times. The interesting
381 consequence of the simple flow line distribution for these springs is that a single flow line can be
382 considered as representative of all the flow lines that are feeding the spring, irrespective of the
383 hydrological conditions. Hydrogeochemical simulations were performed along a single flow line
384 for different hydrological periods using the methodology illustrated in figure 5. The case of CS1
385 spring is used below to highlight the main results obtained from this approach. For the strong
386 flood of 30/03/2010, the KIRMAT simulations modeling the waters coming from the proximity of
387 the spring and characterized by short transit times produced too much diluted solutions,
388 whereas the waters coming from the main crests are too much concentrated to reproduce the
389 spring water chemical composition. However, after an integration of all the waters arriving at
390 CS1 with the different transit times employed for the simulation, the resulting geochemical
391 composition correctly reproduces the chemical composition of CS1 spring water at this date

392 (H_4SiO_4 , Na^+ , K^+ , Mg^{2+} , and Ca^{2+} concentrations, figure 7D). A similar conclusion is obtained for
393 the important drought of 29/11/2011. Again, geochemical integration of all the waters arriving
394 at CS1 along a water line but with different transit times correctly reproduces the chemical
395 composition of the CS1 spring waters collected on this date (figure 7C). This comment applies
396 regardless of the time period considered.

397 The coupled hydrological and hydrogeochemical approach has been applied for the CS1 spring
398 for 6 dates covering the whole range of the water discharges of the spring (table 1). The
399 modeling results capture the seasonal variations of the water chemical composition of the CS1
400 spring over the whole range of observed flow rates at CS1 (figure 8). Simulations especially
401 account for the 20-30% variation in H_4SiO_4 concentrations (figure 8A), the 10-20% variation in
402 Na^+ concentrations (figure 8C), and the relatively stability of the K^+ , Mg^{2+} and pH of the CS1
403 waters (figure 8E, 8F and 8D). The response of each chemical element to a change in water
404 discharge is related to the initial soil solution concentration, the nature of primary minerals
405 controlling its budget and the degree of its incorporation into clay minerals. Specific
406 concentration-mean transit time relations (C-MTT relations) explain why the response of solute
407 concentrations to hydrological changes is different for each element (figure 9). Similar results
408 are obtained for the CS3 spring (figure EA1), showing, as for the CS1 spring, that the model
409 correctly simulates the water chemical composition of the CS3 spring.

410 **5-2 PZ3 and PZ5 piezometers (southern slope)**

411 The two piezometers PZ3 and PZ5 are located on the southern part of the catchment, and their
412 waters drain a granitic bedrock similar to that drained by the CS sources. As for the CS1 and CS3

413 springs, the NIHM modeling results show that the flow lines arriving at the PZ3 piezometer are
414 characterized by a relatively simple distribution. The flow lines are close to each other, and they
415 render similar water velocities on the slopes (figure 4). For the PZ5 piezometer located
416 downstream, the flow lines cover a larger area on the slope, especially during droughts (figure
417 4). However, for a given date, all the flow lines show similar velocities, with particularly fast
418 flows on the lower portion of the hillslope. These results imply that, as for the CS1 and CS3
419 springs, the hydrogeochemical simulations of PZ3 and PZ5 piezometer waters can be performed
420 by relying upon a single flow line representative of all the waters collected by the piezometers
421 on a given date.

422 The geochemical integration along the flow line has been performed in the same manner as
423 detailed above, and this approach is able to reproduce the chemical composition of the waters
424 of the two piezometers, as illustrated in figure 10 for the flood of the 05/05/2015 and in figure
425 EA2 for the dry conditions of 10/11/2015. Together, these modeling results show that the flow
426 along linear or slightly convex slopes on the southern part of the catchment allows to correctly
427 capture the water chemistry of each sampling site with a straightforward integration along a
428 single and representative flow line.

429 **5-3 The CS2 and CS4 springs (in the valley axe)**

430 CS2 and CS4 spring waters drain the same granitic bedrock as the CS1 and CS3 waters, but are
431 located in the direction of the small valley of the Strengbach stream and surrounded by slopes
432 of various orientations and inclinations (figure 4). Consequently, the distribution of the flow
433 lines is much more scattered than for the CS1 and CS3 springs. For the CS2 spring, and for all the

434 hydrological conditions, two different groups of flow lines have been determined by the
435 backtracking approach: a northern group characterized by relatively slow velocities and a
436 southern group with higher velocities (figure 4). When the hydrological conditions vary from a
437 strong flood (30/03/2010) to an important drought (29/11/2011), the flow rates tend to
438 decrease along all the flow lines (figures 11A and 11B). For example, the mean flow velocities
439 along the flow lines vary from approximately 12 m/day to 2 m/day between these two dates.
440 For a given date, the northern group systematically renders slower velocities than the southern
441 group. This scattered distribution of the flow lines implies that a single specific flow line cannot
442 be representative of all the waters collected by the spring. The flow lines calculated using the
443 NIHM model allow for constraining the trajectories of the waters within the watershed;
444 however, the simulations performed in this study cannot provide the mass fluxes of water
445 carried by each flow line. Consequently, a straightforward calculation of the chemistry of the
446 CS2 spring, such as detailed above for CS1, is not applicable because the mixing proportions
447 between the different flow lines are unknown.

448 Alternatively, it is possible to determine the concentrations in the waters carried by the slowest
449 and the fastest flow lines that are feeding the spring and to compare the results with the
450 observed chemistry of the spring water. The results indicate that for all the hydrological
451 conditions, the concentrations calculated from the geochemical integration along the slowest
452 and the fastest flow lines are able to correctly frame the chemical composition in terms of
453 H_4SiO_4 , Na^+ , K^+ , Mg^{2+} , and Ca^{2+} of the CS2 spring waters (results are reported for H_4SiO_4 and Na^+
454 in figures 11C and 11D). The observed chemistry of the CS2 spring is bounded by the chemical
455 compositions of the waters carried by the slowest and fastest flow lines. The modeling results

456 also suggest that the contributions of the slow and fast flow lines are comparable over most of
457 the hydrological conditions, as the observed concentrations are in general at the midpoint
458 between the min (i.e., fast) and max (i.e., slow) boundaries (figures 11C and 11D). It is only for
459 the important droughts that the spring chemistry seems to be mainly controlled by the southern
460 and faster group of flow lines. Further works to precisely estimate the mass fluxes of water
461 carried by each flow line are necessary to model the chemistry of the CS2 spring water with a
462 weighted mixing calculation. The same conclusions apply to the CS4 spring located close to CS2.

463 **5-4 The RH3 spring (northern slope)**

464 The RH3 spring is located on the northern part of the catchment (figure 4), where steep slopes
465 imply fast water velocities and subparallel flow lines. However, if the distribution of the flow
466 lines on the RH3 hillside is simple (as for the CS1 and CS3 springs) the precise lithological nature
467 of the bedrock drained by the RH3 waters is more difficult to constrain (Ackerer et al., 2018).
468 Unlike the southern slope, the bedrock of the northern part of the catchment reveals a complex
469 lithology, with gneiss outcropping in the upper part of the slope and granite of variable degree
470 of hydrothermal overprinting in the intermediate and lower parts. These lithological variations
471 can explain the differences in chemical composition between the RH3 spring waters and the
472 waters of the southern part of the catchment: the RH3 spring waters are characterized by
473 systematically higher concentrations of K^+ and Mg^{2+} cations but show similar concentrations for
474 the other major elements (Ackerer et al., 2018; Pierret et al., 2018). The vertical extension of
475 the gneiss and the spatial variability of the hydrothermal overprinting along the northern slopes
476 are not well known, with the consequence that a straightforward modeling of water chemistry
477 as done for CS1 is not possible for RH3.

478 Alternatively, simulations of two extreme cases can be performed by assuming that the flow
479 lines only run, either on gneiss or on hydrothermally altered granite. When only considering the
480 hydrothermally altered granite (VS facies), the simulated concentrations of H_4SiO_4 and Na^+ are
481 close to the measured ones. Nevertheless, the concentrations of K^+ and especially Mg^{2+} are
482 clearly underestimated (figure 12B). In the case of the flow lines only running on gneiss (GN
483 facies), the simulated concentrations of H_4SiO_4 and Na^+ also match the data. However, due to
484 the higher abundance of biotite in the gneiss, the simulated concentrations of K^+ and Mg^{2+} are
485 higher than the measured ones (figure 12A). At this stage, it is therefore reasonable to propose
486 that the chemical composition of the RH3 spring waters reflects mixing of the two lithological
487 influences. By assuming a geochemical conservative mixing, which is likely a too simplistic
488 scenario, the results would indicate that the flow lines portions running on gneiss and on
489 hydrothermally altered granite count for approximately 40-50% and 50-60% of the total water
490 path length, respectively.

491 Further works to estimate the location of the contact between gneiss and granite are required
492 for more realistic modeling and hence a deeper interpretation of the chemical composition of
493 the RH3 spring waters. In any case, the important point to stress here based on the above
494 simulations is that the complex lithology and bedrock heterogeneity mainly impact the K^+ and
495 the Mg^{2+} budget of the RH3 waters, but not or only slightly the H_4SiO_4 and Na^+ concentrations,
496 which control the main part of global weathering fluxes carried by the Strengbach spring waters.
497 These results readily explain why although the RH3 spring waters exhibits higher Mg^{2+} and K^+
498 concentrations than the other CS springs, they carry relatively similar global weathering fluxes
499 (Viville et al., 2012; Ackerer et al., 2018).

500 **6- Discussion**

501 The coupling of the NIHM and KIRMAT codes allows for building a better modeling scheme to
502 those commonly used in previous studies regarding the hydrogeochemical modeling of surface
503 waters at the watershed scale. In such previous works, the geochemical simulations were
504 performed mainly along a single 1D flow line, only characterized by homogeneous mean
505 hydrological properties (Goddéris et al., 2006; Maher, 2011; Moore et al., 2012; Lucas et al.,
506 2017; Ackerer et al., 2018). In the previous study on the Strengbach watershed (Ackerer et al.,
507 2018), the soil solutions were also assumed to percolate in the bedrock only at a single starting
508 point of the flow lines. Although these previous approaches were useful for determining the
509 long-term evolution of regolith profiles and/or the mean chemistry of waters at the pluri-annual
510 scale, they cannot be used to discuss the seasonal variations of the water chemical composition.
511 The NIHM-KIRMAT coupling approach makes this possible, as it provides the spatial distribution
512 of the flow lines at the watershed scale and their variations over time. Furthermore, the
513 proposed modeling approach also integrates a soil solution percolation scheme with inlets
514 uniformly distributed along the slope, which is more realistic than a scheme assuming that each
515 sampled site is fed by a single flow line carrying waters with a unique transit time. The good
516 agreement between modeling results and observations over a large panel of hydrological
517 conditions gives weight to the conclusions and implications that can be drawn regarding the
518 hydrogeochemical functioning of this headwater catchment.

519 **6-1 Choices of the reactive surfaces and the kinetic constants**

520 For the geochemical simulations performed in this study, the kinetic constants that were used
521 to describe the dissolution reactions of the primary minerals are standard constants determined
522 through laboratory experiments (supplementary table EA12). The reactive surfaces of the
523 primary minerals were calculated by assuming a simple spherical geometry for all the minerals
524 (supplementary table EA10). Over the last years, several studies have suggested that the kinetic
525 constants determined through laboratory experiments overestimate the rates of the dissolution
526 reactions in natural environments (White and Brantley, 2003; Zhu, 2005; Moore et al., 2012;
527 Fischer et al., 2014). The origin of this laboratory-field discrepancy is still a matter of debate
528 (Fischer et al., 2014). Different processes have been proposed to explain the gap between
529 laboratory and field estimates, such as the crystallographic anisotropy (Pollet-Villard et al.,
530 2016), progressive occlusion of the primary minerals by clays (White and Brantley, 2003), or the
531 formation of passivation layers at the surfaces of the minerals (Wild et al., 2016, Daval et al.,
532 2018). The difficulty to reconcile field and laboratory estimates can also be related to the
533 challenge of defining relevant reactive surfaces at different space scales (Li et al., 2006; Navarre-
534 Sitchler and Brantley, 2007).

535 The present modeling work regarding the Strengbach catchment shows that the chemical
536 composition variability of the spring and piezometer waters is fully captured via geometric
537 reactive surfaces and standard kinetic constants, while respecting the water-rock interaction
538 times within the catchment. This result suggests that the mean rates of the weathering
539 reactions employed in this modeling work are realistic, which in turn implies that the modeling
540 approach developed in this study does not underline significant mismatches between field and
541 laboratory reaction rates. The calculated rates of the dissolution reactions depend on the

542 product between the kinetic constants of the reactions and the mineral reactive surfaces. In the
543 experimental studies performed for determining the kinetic constants of dissolution reactions,
544 the constants are usually determined by normalizing the experimental weathering rates with
545 the Brunauer-Emmett-Teller surfaces determined from experiments of gas absorption (BET
546 surfaces; Chou and Wollast, 1986; Lundstrom and Ohman, 1990; Acker and Bricker, 1992;
547 Amrhein and Suarez, 1992; Berger et al., 1994; Guidry and Mackenzie, 2003).

548 In table 3, the BET surfaces are compared with the geometric surfaces of the minerals involved
549 in the dissolution experiments, recalculated from the size ranges of the minerals. For most of
550 the minerals (apatite, quartz, albite, K-feldspar, and anorthite), the geometric surfaces are
551 within the same order of magnitude as the BET surfaces, even if often slightly lower (table 3).
552 However, as the BET surfaces are determined with fairly large uncertainties, especially for low
553 BET surfaces (up to $\pm 70\%$), and as they can be very different depending on the gas used (up to
554 50% of difference between N₂ or Kr absorption; Brantley and Mellott, 2000), the above
555 differences between the geometrical and the BET surfaces cannot be considered significant for
556 the majority of minerals used in the Strengbach simulations. A significant difference only
557 appears for biotite, with the geometric surfaces one order of magnitude less than the BET
558 surfaces (table 3). However, for biotite, due to its layered structure, it has been shown that
559 approximately 80 – 90% of the surface area accessible by the gases used to estimate BET
560 surfaces is not accessible for weathering reactions (Nagy, 1995).

561 The above considerations explain why for a granitic bedrock as found in the Strengbach
562 catchment, the geometric surfaces are relevant to describe the surfaces of water-rock
563 interactions at the space and time scales of this study. An immediate corollary is that the values

564 of the standard kinetic constants (table EA12) are also appropriate to calculate reaction rates
565 with mineral geometric surfaces in our modeling approach. This ability may be related to the
566 fact that all the minerals that have been used in the dissolution experiments and in the kinetic
567 studies were collected in the field (e.g., Acker and Bricker, 1992; Amrhein and Suarez, 1992).
568 These minerals were likely affected by anisotropy, passivation layers, and any types of aging
569 effects related to long-term water-rock interactions. Our results might therefore mean that the
570 standard kinetic constants obtained in such experiments integrate the aging effects that have
571 affected the reactivity of the primary minerals in natural environments. This would explain why
572 it is possible to capture the full variability of the water chemistry in a headwater catchment with
573 simple geometric reactive surfaces and standard kinetic constants.

574 At this stage, the results of our simulations strengthen the idea that the low surfaces calculated
575 from the geometrical shapes of minerals provide good estimates of the reactive surfaces within
576 the natural environment (Brantley and Mellott, 2000; Gautier et al., 2001; White and Brantley,
577 2003; Zhu, 2005; Li et al., 2017). They are certainly the values to be used for hydrogeochemical
578 modeling such as that performed in this work, in addition to the use of the experimental kinetic
579 constants for mineral dissolution. These conclusions are certainly not specific to the Strengbach
580 catchment and could be applicable to many other granitic catchments.

581 **6-2 Implications for the acquisition of the water chemistry**

582 The results of the NIHM-KIRMAT hydrogeochemical modeling have strong implications
583 regarding the hydrogeochemical functioning of the Strengbach watershed. Firstly, the modeling
584 results emphasize the importance of water transit times within the watershed as a main feature

585 controlling the chemical composition of subsurface waters. Along all the slopes, the waters
586 coming from the vicinity of the crests and characterized by long transit times systematically
587 render higher concentrations than the waters with shorter pathways and transit times. When
588 the hydrological conditions change from wet to dry periods, the solute concentrations also tend
589 to increase with the increase in the mean transit time of waters. Our results show that for the
590 spring and piezometer waters, the spatial and temporal variations of their geochemical
591 composition are fully explained by the differences in water transit times (figure 13). Transit time
592 variations between high and low discharge periods explain the temporal variations of
593 geochemical signatures within each site. Various mean transit times of waters supplying the
594 different sites explain the various chemical compositions between the sites (figure 13). This key
595 role of the water-rock interaction time is in agreement with previous reactive-transport studies
596 (e.g. Maher, 2010; Moore et al., 2012; Lebedeva and Brantley; 2013).

597 This study also brings strong constrains on the spatial distribution of the weathering
598 processes. For the modeling strategy employed, the chemical composition of the spring and
599 piezometer waters are calculated by integrating the chemical composition of waters introduced
600 at different starting locations along the active part of the flow lines (figure 5). The modeling
601 results show that through the geochemical integration, the concentrated waters coming from
602 the main crests are naturally counterbalanced by the diluted waters infiltrating close to the
603 sampling sites. This scheme supports the ideas suggested in Ackerer et al. (2016) and in Viville et
604 al. (2012) that the solute chemistry is acquired through reactions and weathering processes that
605 are spatially relatively homogenous along the flow lines of the watersheds. Because the lengths
606 of the flow lines vary with time, the patterns of dissolution rates for primary minerals are mainly

607 controlled by the spatial and temporal variability of the flow lines. During wet conditions, the
608 upper parts of the catchment are the areas of maximal dissolution rates of primary minerals in
609 the regolith. During dry conditions, the dissolution rates are maximal at mid-slopes, as the
610 upper parts of the catchment are simply dry.

611 The NIHM modeling also shows that the hydrological functioning of the watershed is properly
612 simulated by water circulations in the shallow subsurface, i.e., in a saprolitic aquifer. No
613 contribution of waters circulating in the deep fracture network of the granitic bedrock and
614 observed during the drilling campaigns is necessary. The deep-water circulations are probably
615 disconnected from the shallow subsurface network, as recently suggested by geochemical
616 studies conducted in the Strengbach watershed (Chabaux et al., 2017). The modeling results
617 also show that water in the shallow aquifer flows along streamlines with fairly simple
618 geometries. At the scale of the catchment (figure 4), the geometry of the flow lines validates the
619 hypothesis based on the geochemical and Sr-U isotopic data that the spring waters of these
620 mid-mountain basins are supplied by waters from distinct flow paths without real
621 interconnections (i.e., the Strengbach and Ringelbach watersheds; Schaffhauser et al., 2014;
622 Pierret et al., 2018).

623 **6-3- Origins of general chemostatic behavior and of specific C-Q relations**

624 The hydrogeochemical monitoring of the spring, piezometer, and stream waters performed in
625 the Strengbach catchment clearly shows that this catchment has a general chemostatic behavior
626 (e.g., Viville et al., 2012; Ackerer et al., 2018). All the spring and the piezometer waters have
627 chemical concentrations impacted by changes in the hydrological conditions, but the

628 concentration variation ranges are by far narrower than variation ranges of water discharges,
629 which define the chemostatic behavior of a hydrological system. For waters showing the largest
630 concentration variations (spring CS1), there is a modest increase of approximately 10-30% in the
631 concentrations of H_4SiO_4 and Na^+ from floods to drought events, while the water discharges
632 may vary by a factor of 15 (figure 8). This modest variability of the solute concentrations over a
633 wide range of water discharges is not specific to the Strengbach catchment; it has been
634 observed in several watersheds spanning different climates and hydrological contexts (Godsey
635 et al., 2009; Clow and Mast, 2010; Kim et al., 2017).

636 Different origins for the chemostatic behavior have been proposed, such as a
637 modification of the mineral reactive surfaces during changing hydrological conditions (Clow and
638 Mast, 2010), a small concentration difference between slow and fast moving waters (Kim et al.,
639 2017), or the fact of reaching an equilibrium concentration along the water pathway (Maher,
640 2010). The coupled approach NIHM-KIRMAT renews the opportunity to discuss on the origin of
641 the chemostatic behavior in catchments. It is worth noting that the acquisition and the
642 evolution of the water chemistry can be simulated along flow lines that have been determined
643 via timely and spatially distributed hydrological modeling. The strength of this approach is to
644 constrain water transit times independently and before any geochemical simulation.

645 The results from the hydrological model show that the characteristics of the flow lines are
646 affected by the changes in the hydrological conditions. After important precipitations, high
647 water contents and large hydraulic conductivities are simulated in the vicinity of the crests and
648 all along the small valley of the catchment (figure 6). During drought periods, the crest lines
649 have progressively dried out, and the hydraulic conductivities decrease on the upper parts of

650 the watershed. Only some locations at mid-slopes and along the direction of the principal valley
651 exhibit larger hydraulic conductivities (figure 6). This response of the hydraulic conductivities
652 implies that during floods, the water velocity significantly increases along the flow lines, but the
653 length of the active parts of the flow lines also increase as waters collected downstream may
654 also come from the neighborhood of the main crests. During drought periods, the water velocity
655 is slower, but the length of the active parts of the flow lines also tends to decrease, as the
656 waters are principally supplied by mid-slope areas characterized by a thicker aquifer.

657 For illustration, velocities of water supplying the CS1 spring varied along the flow lines between
658 7 and 0.5 m/day during the flood of 30/03/2010 and were approximately 0.5-1 m/day during
659 the important drought of the 29/11/2011 (figure 6). At the same time, the active parts of the
660 flow lines were reduced from 160 m to 110 m from the flood to the drought events (figures 7A
661 and 7B). This hydrological functioning implies a covariation between flow velocity and flow
662 length over changing hydrological conditions, with faster flows along longer paths during wet
663 conditions and slower flows along shorter paths during dry periods. This hydrological behavior
664 attenuates the variations of the water transit times over changing hydrological conditions. It
665 also explains why the mean transit times span much narrower variation ranges than the water
666 discharges at the collected springs. For example, the calculated mean transit times of waters for
667 the CS1 spring vary from 1.75 to 3.13 months between the strongest flood and the driest period
668 that have been studied, whereas the water discharges vary from 1.523 L/s to 0.098 L/s (figure
669 8B). Because the time of the water-rock interactions exerts a first-order control on the chemical
670 composition of waters, the weak variability of the mean transit times is directly responsible for
671 the relative stability of the chemical composition of waters within the catchment.

672 In addition to the general chemostatic behavior, each chemical element has a specific response
673 to a change in water transit time as apparent in figure 9 where are given the concentration-
674 mean transit time relations (C-MTT relations) for H_4SiO_4 and the major cations. In the relevant
675 transit time window for the spring and piezometer waters (figure 9b), the C-MTT relations are
676 linear and C-MTT slopes are significant for H_4SiO_4 , modest for Na^+ and weak for Mg^{2+} and K^+
677 concentrations. Modeling results indicate that the C-MTT slopes are controlled by the
678 competition between primary mineral dissolution and element incorporation into clay minerals.
679 When elemental fluxes from primary mineral dissolution to solution are much higher than fluxes
680 from solution to clay minerals (e.g. H_4SiO_4), the element can accumulate in solution, resulting in
681 a significant C-MTT slope. By contrast, when elemental fluxes from primary mineral dissolution
682 to solution are only slightly higher than fluxes from solution to clay minerals (e.g. K^+), the
683 element accumulates only slowly in solution, resulting in a weak C-MTT slope. Interestingly,
684 when fitting power-laws along C-Q relations ($C=aQ^b$, figure 8 caption), both 'a' coefficient
685 controlling the height of the C-Q laws and 'b' coefficient controlling the curvature of the C-Q
686 laws are sensitive to the C-MTT slopes (figure 9c and 9d). 'a' coefficient is positively correlated
687 with C-MTT slopes while 'b' coefficient is negatively correlated. Solute species with significant C-
688 MTT slopes are more chemodynamic and display higher mean annual concentrations (H_4SiO_4 ,
689 $b(H_4SiO_4)=-0.1$, $a(H_4SiO_4)=10^{-4}$), whereas species with weak C-MTT slopes show low mean
690 annual concentrations and are nearly perfectly chemostatic ($a(Mg^{2+})=10^{-5}$, $b(Mg^{2+})=-0.016$,
691 $a(K^+)=10^{-5}$, $b(K^+)=0$, figures 8, 9c and 9d). Our results show that a better knowledge of C-MTT
692 relations is important to explain the contrasted C-Q shapes of chemical elements.

693 It is important to underline that the hydrological modeling with the NIHM code is
694 performed independently and before any geochemical simulations with the KIRMAT code. The
695 fact that the flow rates are well reproduced for all the hydrological contexts between 2010 and
696 2015 supports that the water transit times inferred from the NIHM code are realistic. The fact
697 that the chemical composition of waters is well captured indicates that the combination of the
698 geochemical parameters used in KIRMAT code is able to generate realistic reaction rates, as
699 chemistry is well reproduced while respecting realistic water transit times. No modifications of
700 the reactive surfaces and of the dissolution kinetic constants were necessary to reproduce the
701 seasonal variability of the water chemistry. It is also important to emphasize that the simulated
702 chemical compositions of waters remain far from a state of chemical equilibrium with respect to
703 primary minerals. The calculated Gibbs free energy for the primary minerals ranges from -120 to
704 -100 kJ/mol for apatite, -90 to -80 kJ/mol for biotite and anorthite and -30 to -20 kJ/mol for
705 albite and K-feldspar. These far-from-equilibrium values for the Gibbs free energy imply that the
706 reaction rates calculated using hydrogeochemical codes such as KIRMAT, which are based on
707 the transient state theory (TST, Eyring, 1935; Murphy and Helgeson, 1987), are realistic for most
708 of the primary minerals in this type of hydrological context. Regarding the simulations
709 performed in this study, the relatively short residence times of waters and the precipitation of
710 clay minerals prevent reaching a state of chemical equilibrium between waters and primary
711 minerals. The results also indicate that relying upon a model of clay solid solution is appropriate
712 to mimic the clay mineral dynamics in this type of watershed and that a clay solid solution
713 precipitated at the thermodynamic equilibrium is able to generate reliable water chemistry (this
714 study) and realistic clay precipitation rates (more details in Ackerer et al., 2018).

715 Our results indicate that it is not necessary to mix in different proportions soil and deep waters
716 to generate chemostatic behavior, as proposed by Zhi et al. (2019). Chemostatic behavior can
717 be generated within a single regolith layer with a homogeneous mineralogy, if as demonstrated,
718 the transit time variability of shallow subsurface waters is dampened by seasonal fluctuations of
719 flow line properties. A large storage of primary minerals and weathering product in the
720 subsurface, as proposed in Musolff et al. (2015), is required but not sufficient to generate
721 chemostatic behavior. Chemostatic behavior also depends on the covariation between flow
722 velocities and flow lengths over changing hydrological conditions. Chemostatic behavior is not
723 explained by a modification of the reactive-surface of minerals in the subsurface (i.e. Clow and
724 Mast, 2010), or by an absence of chemical contrast between slow and rapid flows (i.e. Kim et al.,
725 2017). The precipitation of clay minerals is essential to correctly capture the water chemistry in
726 our study, but the dissolution or redissolution of clays is not a key process to explain
727 chemostatic behavior (i.e. Li et al., 2017). Our study clearly supports the idea defended by
728 Herndon et al. (2018) that a spatial and temporal variability in flow paths is a key process to
729 explain C-Q relations. This conclusion can most likely be extended to the other mountainous and
730 relatively steep watersheds of this type, in which water pathways and short transit times are
731 mainly controlled by gravity driven flow along slopes.

732 **7- Conclusion**

733 This study exemplifies the potential of coupling of low-dimensional and depth-integrated
734 hydrological modeling with hydrogeochemical modeling as a way to better understand
735 variability over time and space of the composition of surface and subsurface waters. The
736 independent estimation of the water transit times provided by hydrological simulations is a

737 clear added value to constrain the geochemical modeling approaches. Our study demonstrates
738 that the seasonal variability of hydraulic conductivities along the slopes is a key process to
739 understand the dynamic of flow lines and the changes of water transit times in the watershed.
740 The variations in flow lines distributions from drought to flood events result in a modest
741 seasonal variability of mean water transit times, which in turn explains the relative stability of
742 the solute concentrations in waters. Our results also show that a better knowledge of the
743 concentration-mean transit time relations (C-MTT relations) is an interesting new step to
744 understand the diversity of C-Q shapes for different chemical elements. The consistency
745 between measured and modeled concentrations while respecting the water-rock interaction
746 times provided by the hydrological simulations shows that it is possible to capture the chemical
747 composition of waters with simply determined reactive surfaces and standard kinetic constants.
748 The results of our simulations strengthen the idea that the low surfaces calculated from the
749 geometrical shapes of minerals are a good estimate of the reactive surfaces within the natural
750 environment and certainly the values to be used for hydrogeochemical modeling such as that
751 performed in this work, in addition to the use of the experimental kinetic constants for mineral
752 dissolution.

753
754 **Acknowledgements:** This work and the Julien Ackerer's salary were financially supported by the
755 French ANR Program (Project CANTARE- Alsace) under grant agreement ANR-15-CE06-0014.
756 This work also benefited from fruitful discussions with D. Daval, and from constructive reviews
757 by two anonymous reviewers and by Laurent Pfister of Luxembourg Institute of Science and
758 Technology (LIST).

759

760 **Bibliography**

- 761 Acker, J. G. and Bricker, O. P.: The influence of pH on biotite dissolution and alteration kinetics at low
762 temperature. *Geochim. Cosmochim. Acta*, 56, 3073-3092, 1992.
- 763 Ackerer, J., Chabaux, F., Van der Woerd, J., Viville, D., Pelt, E., Kali, E., Lerouge, C., Ackerer, P., Di Chiara
764 Roupert, R. and Négrel, P.: Regolith evolution on the millennial timescale from combined U–Th–
765 Ra isotopes and in situ cosmogenic ¹⁰Be analysis in a weathering profile (Strengbach catchment,
766 France). *Earth Planet. Sci. Lett.*, 453, 33-43, 2016.
- 767 Ackerer, J., Chabaux, F., Lucas, Y., Clément, A., Fritz, B., Beaulieu, E Viville D., Pierret, M.C., Gangloff, S.
768 and Négrel, P.: Monitoring and reactive-transport modeling of the spatial and temporal
769 variations of the Strengbach spring hydrochemistry. *Geochim. Cosmochim. Acta*, 225, 17-35,
770 2018.
- 771 Ameli, A. A., Beven, K., Erlandsson, M., Creed, I. F., McDonnell, J. J. and Bishop, K.: Primary weathering
772 rates, water transit times, and concentration-discharge relations: A theoretical analysis for the
773 critical zone. *Water Resour. Res.*, 53, 942-960, 2017.
- 774 Amrhein, C. and Suarez, D. L.: Some factors affecting the dissolution kinetics of anorthite at 25 C,
775 *Geochim. Cosmochim. Acta*, 56, 1815-1826, 1992.
- 776 Bao, C., Li, L., Shi, Y., & Duffy, C.: Understanding watershed hydrogeochemistry: 1. Development of RT-
777 Flux-PIHM. *Water Resources Research*, 53, 2328-2345, 2017.
- 778 Beaulieu, E., Goddérís, Y., Donnadiou, Y., Labat, D. and Roelandt, C.: High sensitivity of the continental-
779 weathering carbon dioxide sink to future climate change, *Nature Climate Change*, 2, 346, 2012.
- 780 Beaulieu, E., Lucas, Y., Viville, D., Chabaux, F., Ackerer, P., Goddérís, Y. and Pierret, M. C. : Hydrological
781 and vegetation response to climate change in a forested mountainous catchment, *Modeling*
782 *Earth Systems and Environment*, 2, 191, 2016.

783 Beisman, J. J., Maxwell, R. M., Navarre-Sitchler, A. K., Steefel, C. I., & Molins, S. ParCrunchFlow: an
784 efficient, parallel reactive transport simulation tool for physically and chemically heterogeneous
785 saturated subsurface environments. *Computational Geosciences*, 19, 403-422, 2015.

786 Berger, G., Cadore, E., Schott, J. and Dove, P. M.: Dissolution rate of quartz in lead and sodium
787 electrolyte solutions between 25 and 300 C: Effect of the nature of surface complexes and
788 reaction affinity, *Geochim. Cosmochim. Acta*, 58, 541-551, 1994.

789 Brantley, S. L. and Mellott, N. P.: Surface area and porosity of primary silicate minerals, *Am. Mineral.*, 85,
790 1767-1783, 2000.

791 Camporese, M., Paniconi, C., Putti, M. and Orlandini, S.: Surface-subsurface flow modeling with path-
792 based runoff routing, boundary condition-based coupling, and assimilation of multisource
793 observation data, *Water Resour. Res.* 46, W02512, doi:10.1029/2008WR007536, 2010.

794 Chabaux, F., Viville, D., Lucas, Y., Ackerer, J., Ranchoux, C., Bosia, C, Pierret, M.C., Labasque, T., Aquilina,
795 L., Wyns, R., Lerouge, C., Dezaye, C. and Négrel, P.: Geochemical tracing and modeling of surface
796 and deep water–rock interactions in first-order granitic watersheds (Strengbach and Ringelbach
797 CZOs, France), *Acta Geochim.*, 36, 363-366, 2017.

798 Chabaux F., Stille P., Prunier J., Gangloff S., Lemarchand D., Morvan G., Négrel J., Pelt E., Pierret M.C.,
799 Rihs S., Schmitt A.D., TrémoièresT., Viville D. Plant-soil-water interactions: Implications from U-
800 Th-Ra isotope analysis in soils, soil solutions and vegetation (Strengbach CZO, France), *Geochim.*
801 *Cosmochim. Acta*, 259, 188-210, 2019.

802 Chorover, J., Derry, L. A., & McDowell, W. H.: Concentration-Discharge Relations in the Critical Zone:
803 Implications for Resolving Critical Zone Structure, Function, and Evolution. *Water Resources*
804 *Research*, 53, 8654-8659, 2017.

805 Chou, L., and Wollast, R.: Steady-state kinetics and dissolution mechanisms of albite. *Am. J. Science*, 285,
806 963-993, 1985.

807 Clow, D. W. and Mast, M. A.: Mechanisms for chemostatic behavior in catchments: implications for CO₂
808 consumption by mineral weathering, *Chem. Geol.*, 269, 40-51, 2010.

809 Diamond, J. S., & Cohen, M. J.: Complex patterns of catchment solute–discharge relationships for coastal
810 plain rivers. *Hydrological processes*, 32, 388-401. 2018.

811 Daval, D., Calvaruso, C., Guyot, F. and Turpault, M. P.: Time-dependent feldspar dissolution rates
812 resulting from surface passivation: Experimental evidence and geochemical implications. *Earth*
813 *Planet. Sci. Lett.*, 498, 226-236, 2018.

814 Ebel, B. A. and Loague, K.: Physics-based hydrologic-response simulation: Seeing through the fog of
815 equifinality. *Hydrological Processes: An International Journal*, 20, 2887-2900, 2006.

816 Eyring, H. The activated complex in chemical reactions. *The Journal of Chemical Physics*, 3, 107-115,
817 1935.

818 Fichter, J., Turpault, M. P., Dambrine, E. and Ranger, J.: Mineral evolution of acid forest soils in the
819 Strengbach catchment (Vosges mountains, NE France), *Geoderma*, 82, 315-340, 1998.

820 Fischer, C., Kurganskaya, I., Schäfer, T. and Lüttge, A.: Variability of crystal surface reactivity: What do we
821 know?, *Appl. Geochem.* 43, 132-157, 2014.

822 Gangloff, S., Stille, P., Schmitt, A.D. and Chabaux F.: Factors controlling the chemical composition of
823 colloidal and dissolved fractions in soil solutions and the mobility of trace elements in soils,
824 *Geochim. Cosmochim. Acta*, 189, 37–57, 2016.

825 Gangloff, S., Stille, P., Pierret, M. C., Weber, T. and Chabaux, F. : Characterization and evolution of
826 dissolved organic matter in acidic forest soil and its impact on the mobility of major and trace
827 elements (case of the Strengbach watershed), *Geochim. Cosmochim. Acta*, 130, 21-41, 2014.

828 Gautier, J. M., Oelkers, E. H. and Schott, J.: Are quartz dissolution rates proportional to BET surface
829 areas?, *Geochim. Cosmochim. Acta*, 65, 1059-1070, 2001.

830 Gérard, F., Clément, A. and Fritz, B.: Numerical validation of a Eulerian hydrochemical code using a 1D
831 multisolute mass transport system involving heterogeneous kinetically controlled reactions, *J.*
832 *Cont. Hydrol.*, 30, 201-216, 1998.

833 Gh'Mari, E. : *Etude minéralogique, pétrophysique et géochimique de dynamique d'altération d'un granite*
834 *soumis aux dépôts atmosphériques acides (bassin versant du Strengbach, Vosges, France).*
835 *Mécanismes, bilans et modélisation*, PhD Thesis, Université Louis Pasteur, Strasbourg, pp. 200.

836 Gislason, S. R., Oelkers, E. H., Eiriksdottir, E. S., Kardjilov, M. I., Gisladottir, G., Sigfusson, B., Snorrason, A.,
837 Elefsen, S., Hardardottir, J., Torssander, P. and Oskarsson, N.: Direct evidence of the feedback
838 between climate and weathering, *Earth Planet. Sci. Lett.*, 277, 213-222, 2009.

839 Goddérés, Y., François, L. M., Probst, A., Schott, J., Moncoulon, D., Labat, D. and Viville, D.: Modelling
840 weathering processes at the catchment scale: the WITCH numerical model, *Geochim.*
841 *Cosmochim. Acta*, 70, 1128–1147, 2006.

842 Goddérés, Y., Brantley, S. L., François, L., Schott, J., Pollard, D., Déqué, M. and Dury, M.: Rates of
843 consumption of atmospheric CO₂ through the weathering of loess during the next 100 yr of
844 climate change, *Biogeosciences*, 10, 135-148, 2013.

845 Godsey, S. E., Kirchner, J. W., and Clow, D. W.: Concentration–discharge relationships reflect chemostatic
846 characteristics of US catchments. *Hydrological Processes: An International Journal*, 23, 1844-
847 1864, 2009.

848 Guidry, M. W. and Mackenzie, F. T.: Experimental study of igneous and sedimentary apatite dissolution:
849 control of pH, distance from equilibrium, and temperature on dissolution rates, *Geochim.*
850 *Cosmochim. Acta*, 67, 2949-2963, 2003.

851 Gunduz, O. and Aral, M. M.: River networks and groundwater flow: a simultaneous solution of a coupled
852 system, *J. Hydrol.*, 301, 216-234, 2005.

853 Gupta, H.V., Kling, H., Yilmaz, K.K., Martinez, G.F. Decomposition of the mean squared error and NSE
854 performance criteria: Implications for improving hydrological modelling. *J. Hydrol.* 377, 80–91,
855 2009.

856 Hazenberg, P., Broxton, P., Gochis, D., Niu, G. Y., Pangle, L. A., Pelletier, J. D., ... and Zeng, X. (2016).
857 Testing the hybrid-3-D hillslope hydrological model in a controlled environment, *Wat. Resour.*
858 *Res.*, 52, 1089-1107, 2016.

859 Herndon, E. M., Steinhofel, G., Dere, A. L., & Sullivan, P. L.: Perennial flow through convergent hillslopes
860 explains chemodynamic solute behavior in a shale headwater catchment. *Chem. Geol.*, 493, 413-
861 425, 2018.

862 Jeannot, B., Weill, S., Eschbach, D., Schmitt, L. and Delay, F.: A low-dimensional integrated subsurface
863 hydrological model coupled with 2-D overland flow: Application to a restored fluvial
864 hydrosystem (Upper Rhine River–France), *J. Hydrol.*, 563, 495-509, 2018.

865 Kampf, S. K. and Burges, S. J.: A framework for classifying and comparing distributed hillslope and
866 catchment hydrologic models, *Water Resour. Res.*, W05423, doi:10.1029/2006WR005370, 2007

867 Kim, H., Dietrich, W. E., Thurnhoffer, B. M., Bishop, J. K. and Fung, I. Y.: Controls on solute concentration-
868 discharge relationships revealed by simultaneous hydrochemistry observations of hillslope
869 runoff and stream flow: The importance of critical zone structure, *Water Resour. Res.*, 53, 1424-
870 1443, 2017.

871 Kirchner, J. W.: Getting the right answers for the right reasons: Linking measurements, analyses, and
872 models to advance the science of hydrology, *Water Resour. Res.* 42, W03S04,
873 doi:10.1029/2005WR004362, 2006.

874 Lebedeva, M. I. and Brantley, S. L. : Exploring geochemical controls on weathering and erosion of convex
875 hillslopes: Beyond the empirical regolith production function. *Earth Surface Processes and*
876 *Landforms*, 38, 1793-1807, 2013.

877 Li, D. D., Jacobson, A. D. and McInerney, D. J.: A reactive-transport model for examining tectonic and
878 climatic controls on chemical weathering and atmospheric CO₂ consumption in granitic regolith.
879 *Chem. Geol.*, 365, 30-42, 2014.

880 Li, L., Peters, C. A. and Celia, M. A.: Upscaling geochemical reaction rates using pore-scale network
881 modeling. *Advances in water resources*, 29, 1351-1370, 2006.

882 Li, L., Bao, C., Sullivan, P. L., Brantley, S., Shi, Y., & Duffy, C. Understanding watershed
883 hydrogeochemistry: 2. Synchronized hydrological and geochemical processes drive stream
884 chemostatic behavior. *Water Resour. Res.*, 53, 2346-2367, 2017.

885 Li, L., Maher, K., Navarre-Sitchler, A., Druhan, J., Meile, C., Lawrence, C., ... and Jin, L. : Expanding the role
886 of reactive transport models in critical zone processes. *Earth-Science Reviews*, 165, 280-301,
887 2017

888 Lucas, Y., Schmitt, A. D., Chabaux, F., Clément, A., Fritz, B., Elsass, P. and Durand, S.: Geochemical tracing
889 and hydrogeochemical modelling of water–rock interactions during salinization of alluvial
890 groundwater (Upper Rhine Valley, France), *Appl. Geochem.*, 25, 1644-1663, 2010.

891 Lucas, Y., Chabaux, F., Schaffhauser, T., Fritz, B., Ambroise, B., Ackerer, J. and Clément, A.:
892 Hydrogeochemical modeling (KIRMAT) of spring and deep borehole water compositions in the
893 small granitic Ringelbach catchment (Vosges Mountains, France), *Appl. Geochem.*, 87, 1-21,
894 2017.

895 Lundström, U. and Öhman, L. O.: Dissolution of feldspars in the presence of natural, organic solutes,
896 *Journal of Soil Science*, 41, 359-369, 1990.

897 Maher, K., Steefel, C. I., White, A. F., & Stonestrom, D. A.: The role of reaction affinity and secondary
898 minerals in regulating chemical weathering rates at the Santa Cruz Soil Chronosequence,
899 California, *Geochim. Cosmochim. Acta*, 73, 2804-2831, 2009.

900 Maher, K. : The dependence of chemical weathering rates on fluid residence time, *Earth Planet. Sci. Lett.*,
901 294, 101-110, 2010.

902 Maher, K.: The role of fluid residence time and topographic scales in determining chemical fluxes from
903 landscapes, *Earth Planet. Sci. Let.*, 312, 48-58, 2011.

904 Mirus, B. B., Ebel, B. A., Heppner, C. S. and Loague, K.: Assessing the detail needed to capture rainfall-
905 runoff dynamics with physics-based hydrologic response simulation, *Water Resour. Res.*, 47,
906 W00H10, doi:10.1029/2010WR009906, 2011

907 Moore, J., Lichtner, P. C., White, A. F. and Brantley, S. L.: Using a reactive transport model to elucidate
908 differences between laboratory and field dissolution rates in regolith, *Geochim. Cosmochim.*
909 *Acta*, 93, 235-261, 2012.

910 Murphy, W. M., & Helgeson, H. C. Thermodynamic and kinetic constraints on reaction rates among
911 minerals and aqueous solutions. III. Activated complexes and the pH-dependence of the rates of
912 feldspar, pyroxene, wollastonite, and olivine hydrolysis. *Geochim. Cosmochim. Acta*, 51, 3137-
913 3153, 1987.

914 Nagy, K. L., White, A. F., & Brantley, S. L. Chemical weathering rates of silicate minerals. *Mineralogical*
915 *Society of America. Washington. DC.* 1995.

916 Navarre-Sitchler, A. and Brantley, S.: Basalt weathering across scales, *Earth Planet. Sci. Let.*, 261, 321-
917 334, 2007.

918 Navarre-Sitchler, A., Steefel, C. I., Yang, L., Tomutsa, L. and Brantley, S. L.: Evolution of porosity and
919 diffusivity associated with chemical weathering of a basalt clast, *Journal of Geophysical Research:*
920 *Earth Surface*, *114*, F02016, doi:10.1029/2008JF001060, 2009.

921 Ngo, V. V., Delalande, M., Clément, A., Michau, N. and Fritz, B.: Coupled transport-reaction modeling of
922 the long-term interaction between iron, bentonite and Callovo-Oxfordian claystone in
923 radioactive waste confinement systems., *Applied Clay Science*, *101*, 430-443, 2014

924 Pan, Y., Weill, S., Ackerer, P. and Delay, F.: A coupled stream flow and depth-integrated subsurface flow
925 model for catchment hydrology, *Journal of Hydrology*, *530*, 66-78, 2015

926 Pierret, M. C., Cotel, S., Ackerer, P., Beaulieu, E., Benarioumlil, S., Boucher, M., ... & Friedmann, P.: The
927 Strengbach catchment: A multidisciplinary environmental sentry for 30 years. *Vadose Zone*
928 *Journal*, *17*, 2018.

929 Pollet-Villard, M., Daval, D., Ackerer, P., Saldi, G. D., Wild, B., Knauss, K. G. and Fritz, B.: Does
930 crystallographic anisotropy prevent the conventional treatment of aqueous mineral reactivity? A
931 case study based on K-feldspar dissolution kinetics, *Geochim. Cosmochim. Acta*, *190*, 294-308,
932 2016.

933 Prunier, J., Chabaux, F., Stille, P., Gangloff, S., Pierret, M. C., Viville, D. and Aubert, A. : Geochemical and
934 isotopic (Sr, U) monitoring of soil solutions from the Strengbach catchment (Vosges mountains,
935 France): Evidence for recent weathering evolution, *Chem. Geol.*, *417*, 289-305, 2015.

936 Schaffhauser, T., Chabaux, F., Ambroise, B., Lucas, Y., Stille, P., Reuschlé, T., Perrone, T. and Fritz, B.:
937 Geochemical and isotopic (U, Sr) tracing of water pathways in the granitic Ringelbach catchment
938 (Vosges Mountains, France), *Chem. Geol.*, *374*, 117-127, 2014.

939 Schmitt, A.D., Gangloff, S., Labolle, F., Chabaux, F. and Stille, P.: Ca biogeochemical cycle at the beech
940 tree - soil solution interface from the Strengbach CZO (NE France): insights from stable Ca and
941 radiogenic Sr isotopes, *Geochim. Cosmochim. Acta* *213*, 91-109, 2017

942 Schmitt AD, Borrelli N., Ertlen D., Gangloff S., Chabaux, F. and Osterrieth M.: Stable calcium isotope
943 speciation and calcium oxalate production within beech tree (*Fagus sylvatica* L.) organs,
944 *Biogeochemistry*, 137,197-217, DOI 10.1007/s10533-017-0411-0, 2018.

945 Steefel, C. I., DePaolo, D. J. and Lichtner, P. C.: Reactive transport modeling: An essential tool and a new
946 research approach for the Earth sciences, *Earth Planet. Sci. Let.*, 240, 539-558, 2005

947 Tardy, Y. and Fritz, B.: An ideal solid solution model for calculating solubility of clay minerals, *Clay*
948 *minerals*, 16, 361-373, 1981.

949 Viville, D., Chabaux, F., Stille, P., Pierret, M. C. and Gangloff, S.: Erosion and weathering fluxes in granitic
950 basins: the example of the Strengbach catchment (Vosges massif, eastern France), *Catena*, 92,
951 122-129, 2012.

952 Weill, S., Altissimo, M., Cassiani, G., Deiana, R., Marani, M. and Putti, M.: Saturated area dynamics and
953 streamflow generation from coupled surface–subsurface simulations and field observations,
954 *Advances in water resources*, 59, 196-208, 2013.

955 Weill, S., Delay, F., Pan, Y. and Ackerer, P.: A low-dimensional subsurface model for saturated and
956 unsaturated flow processes: ability to address heterogeneity, *Computational Geosciences*, 21,
957 301-314, 2017.

958 White, A. F. and Brantley, S. L.: The effect of time on the weathering of silicate minerals: why do
959 weathering rates differ in the laboratory and field?, *Chem. Geol.*, 202, 479-506, 2003.

960 Wild, B., Daval, D., Guyot, F., Knauss, K. G., Pollet-Villard, M. and Imfeld, G.: pH-dependent control of
961 feldspar dissolution rate by altered surface layers, *Chem. Geol.*, 442, 148-159, 2016.

962 Zhi, W., Li, L., Dong, W., Brown, W., Kaye, J., Steefel, C., & Williams, K. H. Distinct Source Water
963 Chemistry Shapes Contrasting Concentration-Discharge Patterns. *Water Resources Research*.
964 2019.

965 Zhu, C.: In situ feldspar dissolution rates in an aquifer, *Geochim. Cosmochim. Acta*, 69, 1435-1453, 2005.

966

967

968 **Figure captions**

969 Figure 1: sampling locations within the Strengbach catchment. Blue stars represent springs, blue
970 diamonds represent piezometers, and the blue circle represents the stream at the outlet of the
971 watershed. Green circles represent soil solution locations, and black diamonds represent
972 bedrock facies locations.

973 Figure 2: on the left: field of thicknesses of the weathered material constituting the shallow
974 unconfined aquifer at the Strengbach catchment used for the simulations by NIHM. The 1D
975 surface draining network used in NIHM is represented by the black lines. On the right: fitting
976 observed flow rates from the Strengbach stream at the outlet of the catchment with simulations
977 of flow within the watershed (illustrated from 2010 to 2015). The subsurface compartment
978 inherits from the aquifer thicknesses reported in the left panel, and the topography makes the
979 natural outlet of the subsurface compartment the surface draining network.

980 Figure 3: principle of the method of backtracking used to determine flow lines that generate
981 flow at the outlet of the Strengbach catchment. Particles are dispatched along the wet fraction
982 of the 1D river network (only one is represented here at a position α on 01/01/2010 at 23:59).
983 NIHM generates an output heterogeneous velocity field at that date for the whole watershed,
984 denoted $V_{01/01/2010}$. By using a velocity field of the same magnitude but opposite direction to the
985 particle, the position of the particle is backtracked until 31/12/2009 23:59. Then, to further
986 backtrack the trajectory of the particle, the velocity field is updated accordingly. The frequency
987 of velocity field updates is set to one day.

988

989 Figure 4: at the top, flow lines of the subsurface that feed with water the surface draining
990 network on March 1st, 2010 (on the left, high-flow period) and July 1st, 2010 (on the right, low-
991 flow period). The color scale indicates that a water particle reaching the river at a given date
992 started its travel along the streamline or passed at a given location on the streamline x days
993 prior. The density of streamlines is associated with the flowing versus dry fraction of the river
994 network at a prescribed date. Below, flow lines of the subsurface that feed with water the
995 geochemical sampling sites on March 30th, 2010 (on the left, flood event) and November 29th,
996 2011 (right, drought event) according to NIHM simulations. For each sampling site, 10 particles
997 were dispatched in the direct neighborhood of the site and then backtracked. The color scale for
998 times is similar to that of the top plot.

999 Figure 5: conceptual scheme used in the modeling of the water chemistry. The soil solutions are
1000 used as input solution. The bedrock is discretized into a 1D succession of cells along the active
1001 parts of the flow lines determined the NIHM hydrological model. The hydrogeochemical model
1002 KIRMAT evaluates reactive transport within each cell. The integrated chemistry of sampled
1003 waters is the arithmetic mean of solute concentrations with regularly distributed inlet points
1004 along a stream line.

1005 Figure 6: maps of piezometric gradient and mean hydraulic conductivity for the Strengbach
1006 catchment, as simulated by NIHM, on 29/11/2011 (dry period) and 30/03/2010 (high flows
1007 period). The mean hydraulic conductivity is integrated normal to bedrock of the aquifer and
1008 thus depends on the water saturation of the vadose zone and the location of the water table.

1009

1010 Figure 7: simulation results for the CS1 spring for an important drought (29/11/2011) and a
1011 strong flood event (30/03/2010). At the top, active parts of the flow lines bringing the waters to
1012 the CS1 spring for the two sampling dates (7A and 7B). Below, simulated chemical compositions
1013 of CS1 spring waters after integration along the flow lines and comparison with the initial soil
1014 solution and the spring chemistry data (7C and 7D). Error bars show analytical uncertainties on
1015 measured concentrations and induced uncertainties in model results.

1016 Figure 8: simulation results for the CS1 spring over the whole range of the water discharges
1017 from the spring. Results are presented for H_4SiO_4 , Na^+ , K^+ and Mg^{2+} concentrations (8A, 8C, 8E
1018 and 8F), pH (8D) and mean water transit time (8B). Red lines indicate simulated parameters
1019 after integration along the flow lines, and blue points show measured values collected between
1020 2005 and 2015 (data in table 1 and in supplementary table EA1). Error bars show analytical
1021 uncertainties on measured concentrations and induced uncertainties in model results. Fitting a
1022 power law of type $C=a*Q^b$ along the C-Q relations gives the following parameters: $a(\text{H}_4\text{SiO}_4)=10^4$,
1023 $b(\text{H}_4\text{SiO}_4)=-0.1$; $a(\text{Na}^+)=7\times 10^{-5}$, $b(\text{Na}^+)=-0.053$; $a(\text{Mg}^{2+})=10^{-5}$, $b(\text{Mg}^{2+})=-0.016$; $a(\text{K}^+)=10^{-5}$,
1024 $b(\text{K}^+)=0$.

1025 Figure 9: (9A) evolution of solute concentrations for H_4SiO_4 , Na^+ , K^+ , Mg^{2+} and Ca^{2+} as a function
1026 of mean water transit time in the Strengbach watershed. Water transit times are between 1.75
1027 and 4 months for all the springs and piezometers in this study. (9B) Focus on the transit time
1028 window (1.75-4 months) for the studied waters and equations linking mean water transit times
1029 and concentrations for H_4SiO_4 , Na^+ , K^+ , Mg^{2+} and Ca^{2+} . Relations between transit times and
1030 concentrations are linear within this window (9C) relations between 'b' coefficients ($C=a*Q^b$)
1031 and the concentration-transit time slopes for the chemical elements. (9D) relations between 'a'

1032 coefficients ($C=a*Q^b$) and the concentration-transit time slopes for the chemical elements.
1033 Elements with significant concentration-mean transit time slopes are slightly chemodynamic
1034 (e.g. H_4SiO_4 and Na^+), while elements with low concentration-mean transit time slopes are
1035 almost chemostatic in the watershed (e.g. K^+ and Mg^{2+}). Ca^{2+} is not shown on 9C and 9D figures
1036 as this element is affected by a strong multi-annual concentration decrease that prevents a
1037 meaningful C-Q power law analysis.

1038 Figure 10: simulation results for the PZ3 and PZ5 piezometers for a flood event (05/05/2015). At
1039 the top, active parts of the flow lines that bring waters to the two sampling sites (10A and 10B).
1040 Below, simulated chemical compositions of the piezometer waters after integration along the
1041 flow lines and comparison with the initial soil solution and the water chemistry data (10C and
1042 10D). Error bars show analytical uncertainties on measured concentrations and induced
1043 uncertainties in model results.

1044 Figure 11: simulation results for the CS2 spring. At the top, active parts of the flow lines that
1045 bring water to the CS2 spring for drought (29/11/2011) and flood (30/03/2010) events (11A and
1046 11B). The CS2 location results in more scattered flow lines than for CS1 spring. Below,
1047 simulation results for the CS2 spring over the whole range of experienced discharges (11C and
1048 11D). Blue lines indicate simulated parameters after integration along the slowest flow line,
1049 yellow lines indicate simulated parameters after integration along the fastest flow line, and blue
1050 points show measured values collected between 2005 and 2015 (data in table 1 and in
1051 supplementary table EA2). Error bars show analytical uncertainties on measured concentrations
1052 and induced uncertainties in model results.

1053 Figure 12: simulation results for the RH3 spring chemistry and for a flood event (30/03/2010).
1054 Left, simulated concentrations by assuming flow lines running through gneiss (GN) only (12A).
1055 Right, simulated concentrations by assuming flow lines running through hydrothermally altered
1056 granite (VS) only (12B). Error bars show analytical uncertainties on measured concentrations
1057 and induced uncertainties in model results.

1058 Figure 13: overview of the simulated flow lines in the subsurface that feed with water the
1059 geochemical sampling sites CS1, PZ3, and PZ5 on May 5th, 2015. The simulated chemical
1060 compositions after geochemical integration along the flow lines are compared with the initial
1061 soil solution and the spring chemistry data.

1062 Table 1: measured pH, water discharges and chemical concentrations of H_4SiO_4 , Na^+ , K^+ , Mg^{2+} ,
1063 and Ca^{2+} in waters collected at the Strengbach catchment. The sampling sites include springs
1064 (CS1, CS2, RH3) and piezometers (PZ3, PZ5).

1065 Table 2: Initial and calibrated values of the hydrodynamic parameters of the aquifer in the
1066 hydrological simulation of the Strengbach catchment by NIHM.

1067 Table 3: Comparison between BET surfaces and geometric surfaces for the major primary
1068 minerals present in a granitic context. BET surfaces were measured via gas absorption
1069 experiments by ¹Berger et al., 1994; ²Chou and Wollast, 1985; ³Lundstrom and Ohman, 1990; ⁴
1070 Amrhein and Suarez, 1992; ⁵Acker and Bricker, 1992; and ⁶Guidry and Mackenzie, 2003.
1071 Geometric surfaces were recalculated from the granulometric ranges of the minerals and by
1072 assuming a spherical geometry.

	Na⁺ (mmol/L)	K⁺ (mmol/L)	Mg²⁺ (mmol/L)	Ca²⁺ (mmol/L)	H₄SiO₄ (mmol/L)	pH	Water Discharge (L/s)
Spring CS1							
16/09/2008	0.071	0.013	0.017	0.044	0.129	6.28	0.954
30/03/2010	0.074	0.014	0.015	0.043	0.120	5.61	1.523
29/03/2011	0.074	0.013	0.015	0.038	0.145	6.23	0.345
04/10/2011	0.080	0.012	0.016	0.042	0.176	6.57	0.122
29/11/2011	0.088	0.015	0.019	0.034	0.177	6.30	0.098
05/05/2015	0.065	0.012	0.012	0.054	0.121	5.33	1.410
Spring CS2							
30/03/2010	0.090	0.020	0.020	0.080	0.122	6.15	6.274
29/03/2011	0.090	0.020	0.020	0.070	0.144	6.18	0.956
02/08/2011	0.090	0.020	0.020	0.060	0.170	6.50	2.171
04/10/2011	0.100	0.020	0.020	0.070	0.177	6.76	0.413
29/11/2011	0.100	0.020	0.020	0.060	0.180	6.22	0.285
05/05/2015	0.077	0.016	0.018	0.074	0.123	6.14	7.500
Spring RH3							
30/03/2010	0.083	0.028	0.032	0.081	0.127	6.28	-
Piezometer PZ3							
05/05/2015	0.074	0.013	0.011	0.053	0.153	6.29	-
Piezometer PZ5							
05/05/2015	0.072	0.013	0.017	0.058	0.132	6.16	-

Table 1

Parameter	Unit	Initial Value	Calibrated value
Depth of substratum	m	4	See figure 2
Saturated hydraulic conductivity (all zones except the low depth zone at the catchment peak (see figure 2))	m.s ⁻¹	1.10 ⁻⁴	8.10 ⁻⁵
Saturated hydraulic conductivity (catchment peak)	m.s ⁻¹	1.10 ⁻⁴	1.10 ⁻⁴
porosity (all zones except the low depth zone at the catchment peak)	-	0.1	0.08
Porosity (catchment peak)	-	0.1	0.2
Residual water content (all zones)	-	0.01	0.01
Specific storage (all zones)	m ⁻¹	1.10 ⁻⁸	1.10 ⁻⁸
n (Van genuchten coefficient, all zones)	-	2	2
α (Van genuchten coefficient, all zones)	m ⁻¹	1	1.5

Table 2

Mineral	Mineral density (g/cm³)	Granulometric range (μm)	Particle radius (μm)	Spherical geometric surface (m²/g)	BET surface (m²/g)
Quartz ¹	2.62	< 50	1 - 25	1.150 - 0.046	0.310
Albite ²	2.60	50 - 100	25 - 50	0.046 - 0.023	0.075
K-feldspar ³	2.56	< 50	1 - 25	1.170 - 0.047	1.420
Anorthite ⁴	2.73	20 - 50	10 - 25	0.044 - 0.111	0.500
Biotite ⁵	3.09	150 - 400	75 - 200	0.013 - 0.005	0.240
Apatite ⁶	3.19	100 - 200	50 - 100	0.018 - 0.009	0.026

Table 3

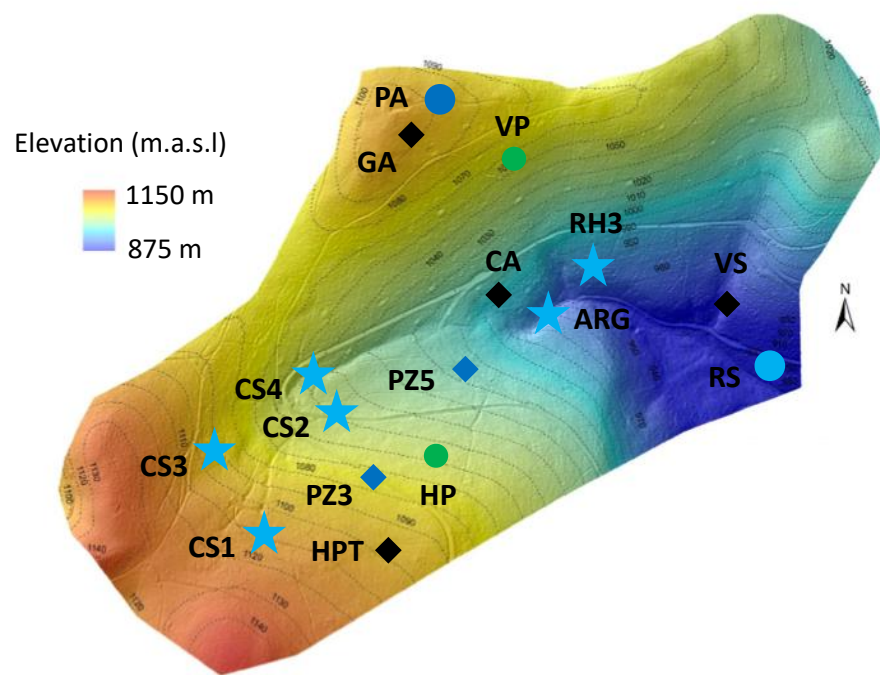


Figure 1

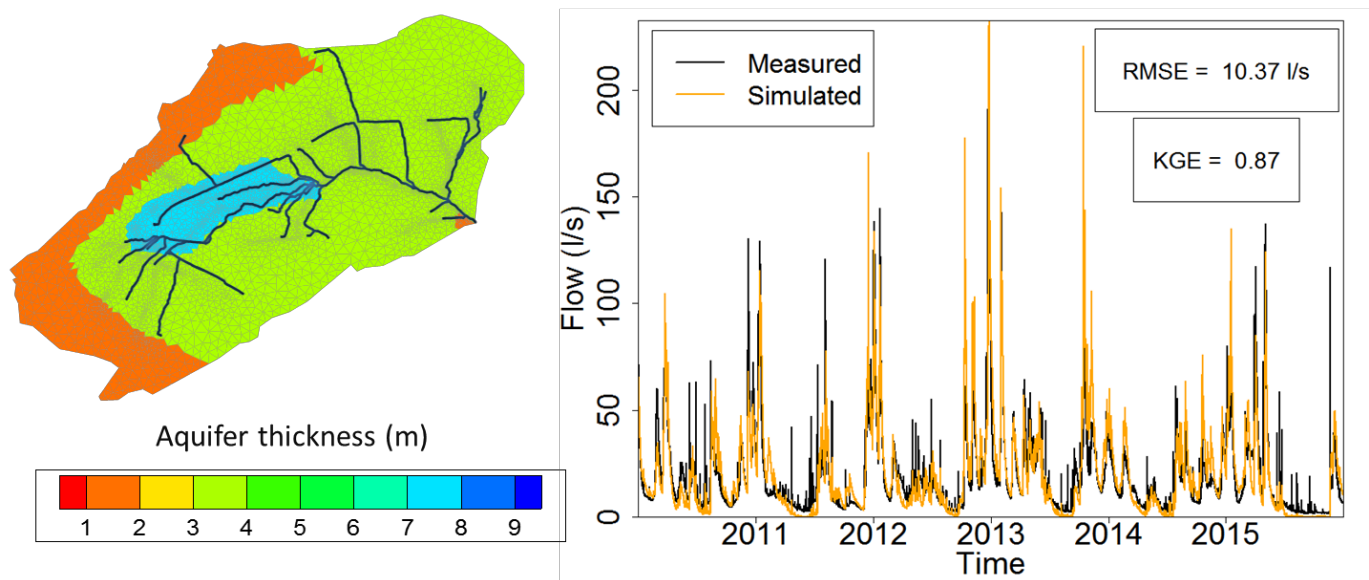


Figure 2

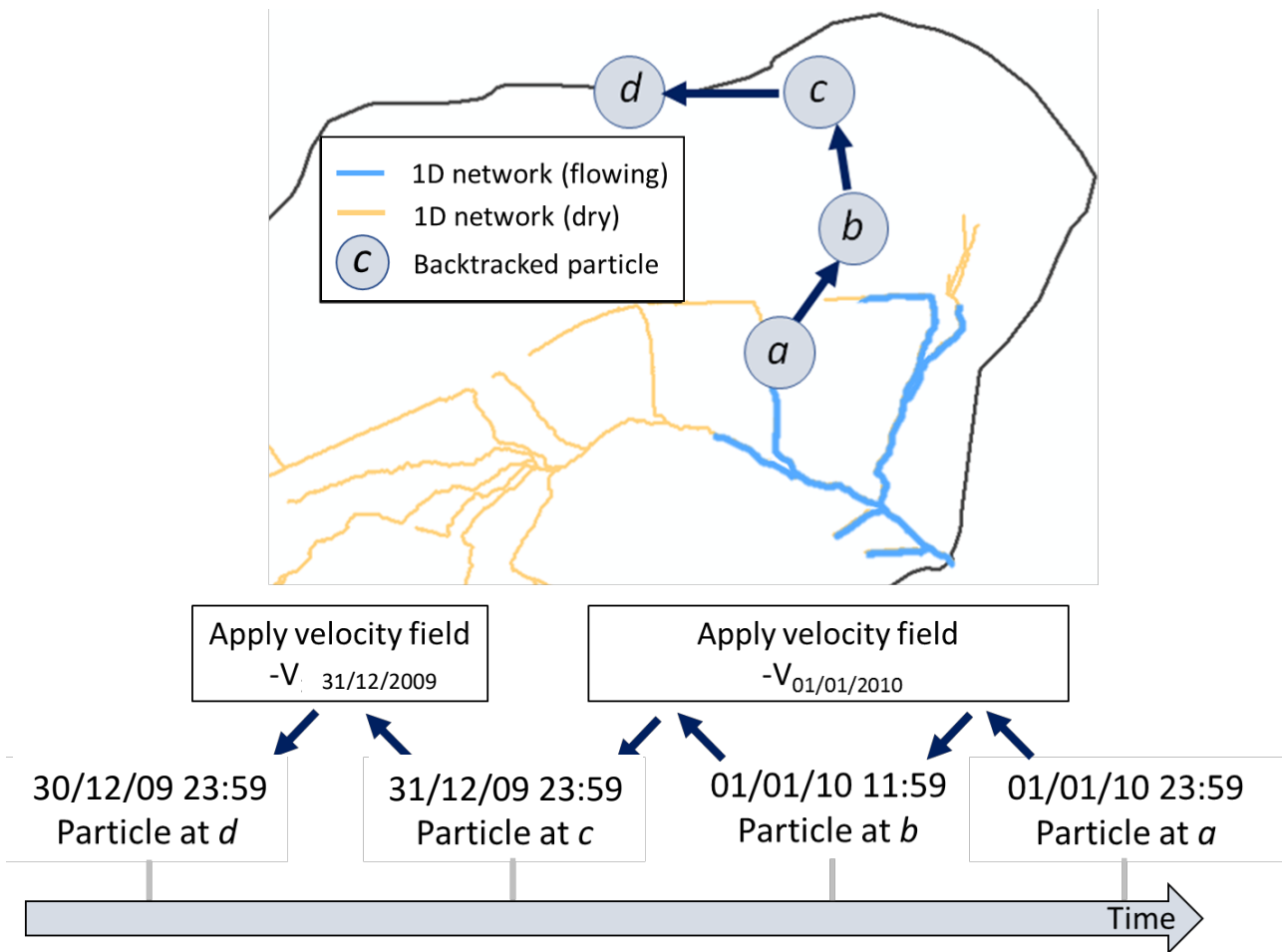


Figure 3

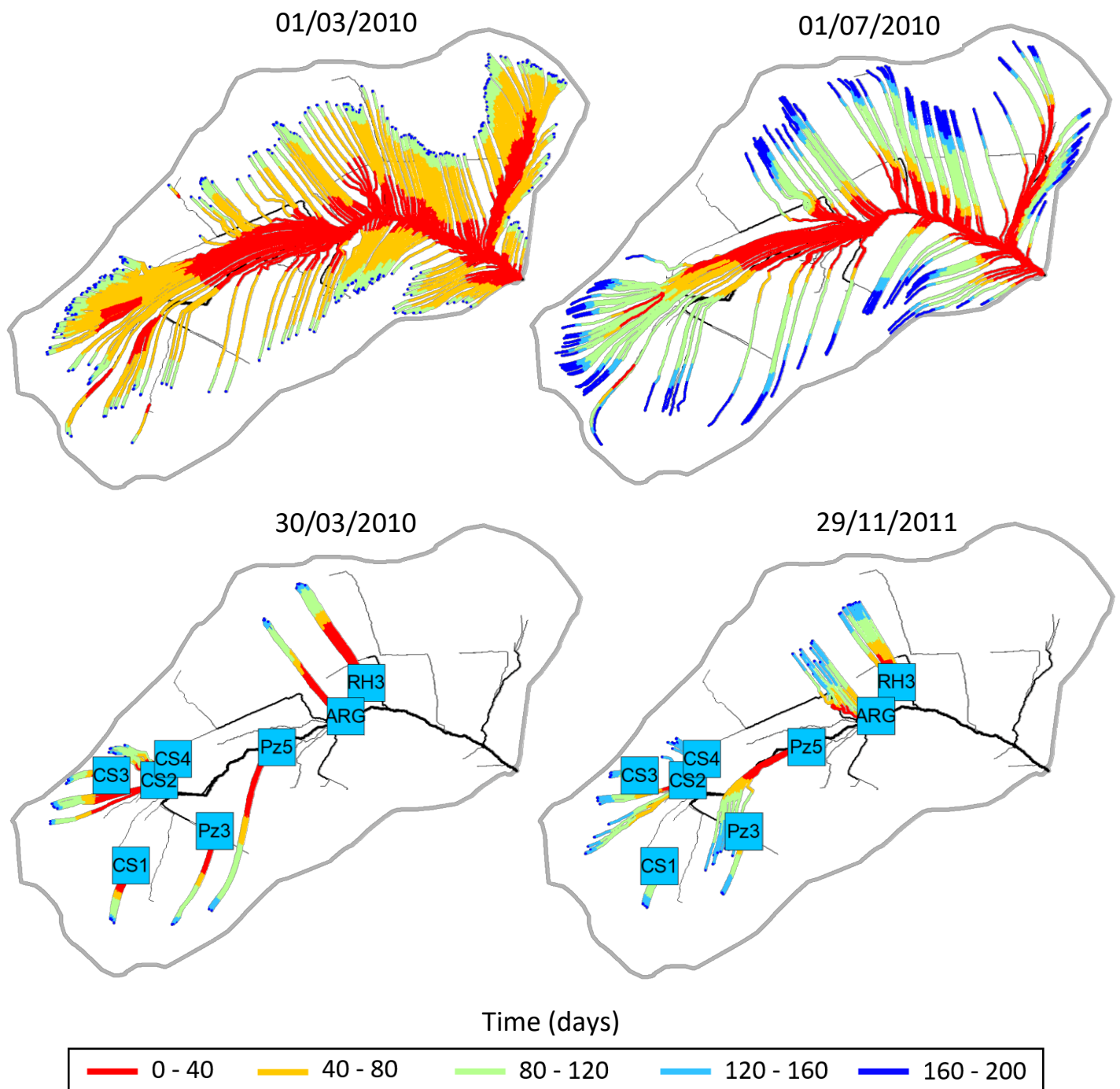


Figure 4

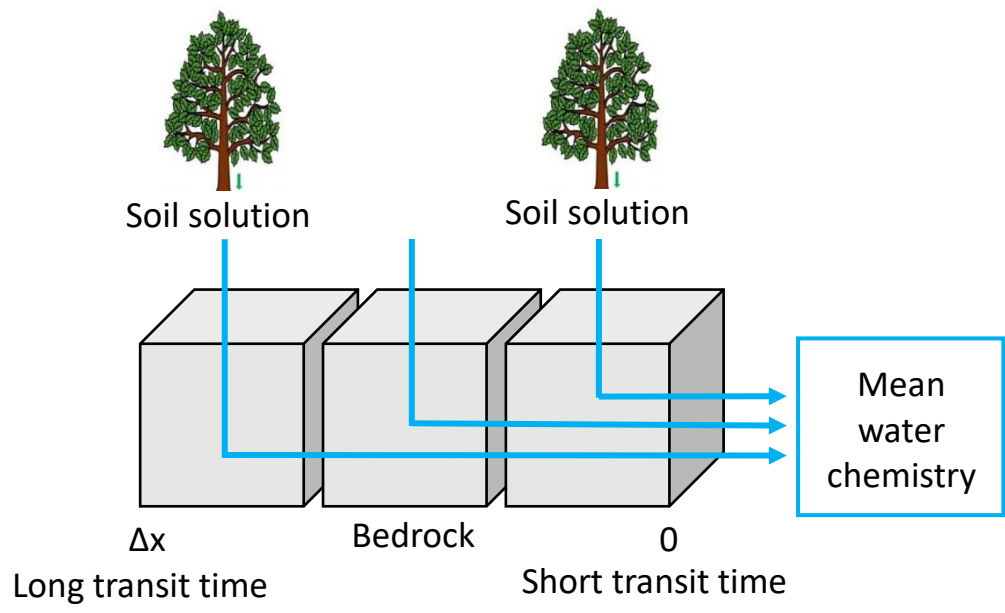


Figure 5

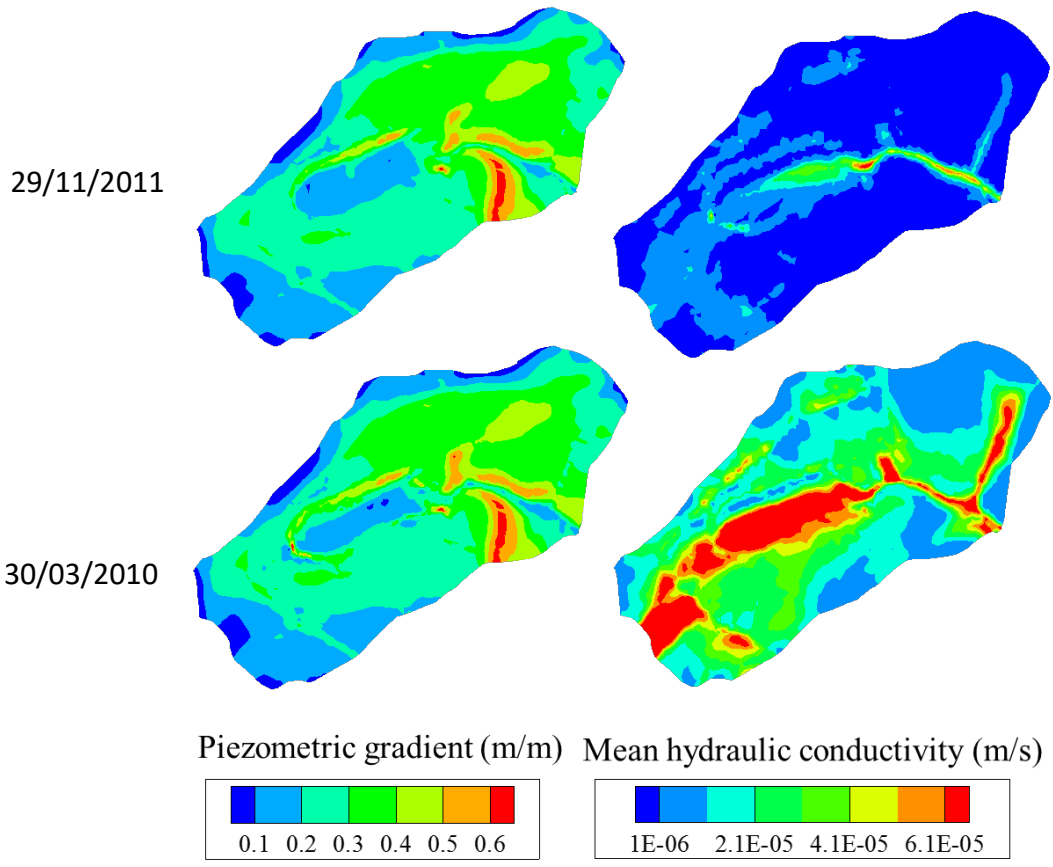


Figure 6

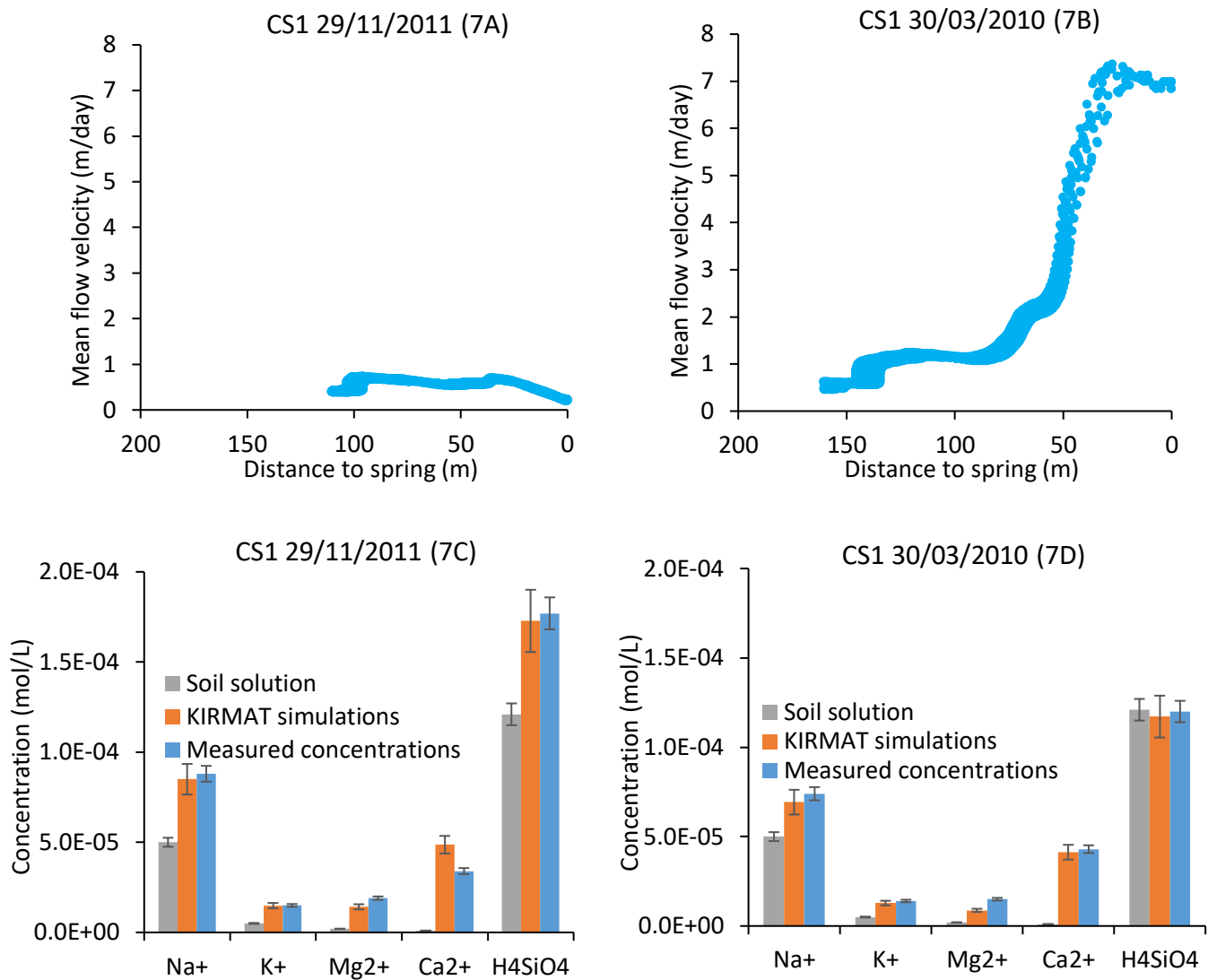


Figure 7

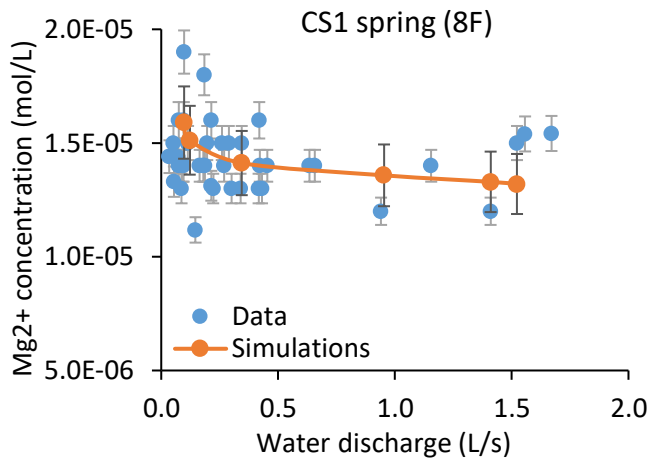
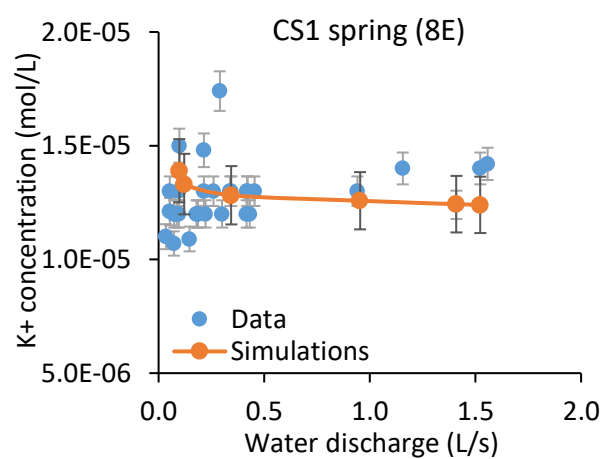
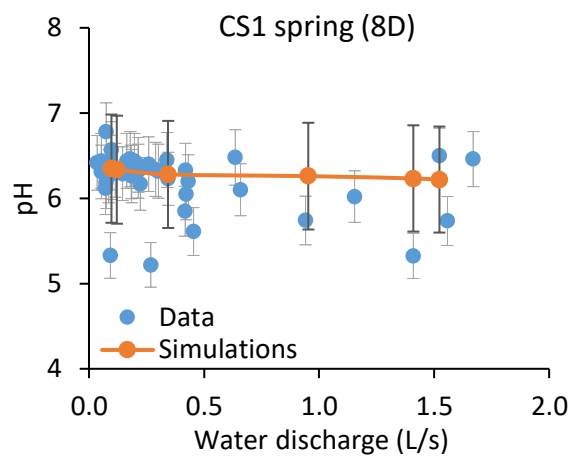
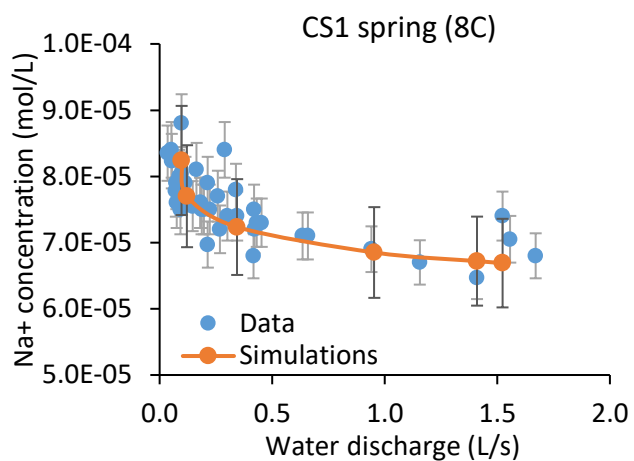
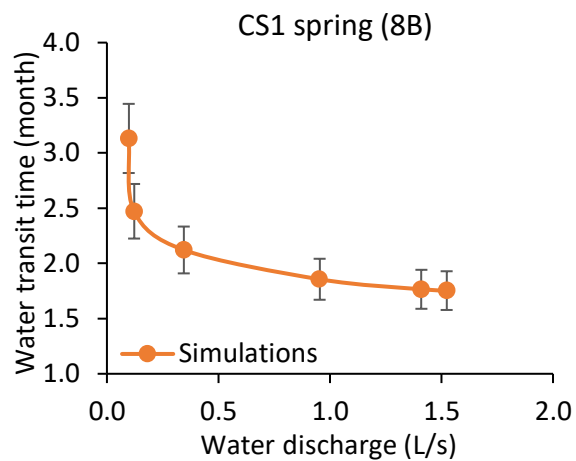
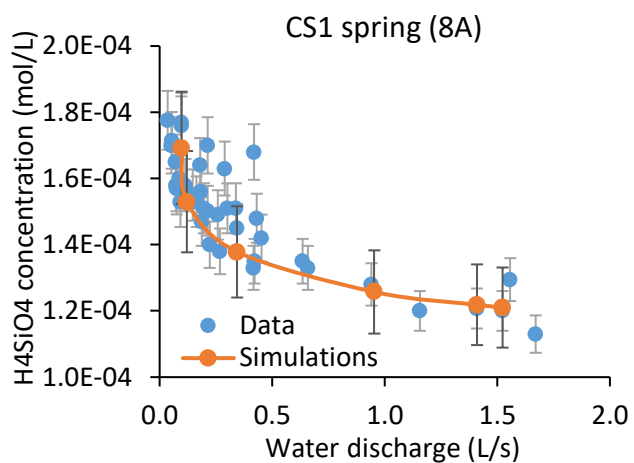


Figure 8

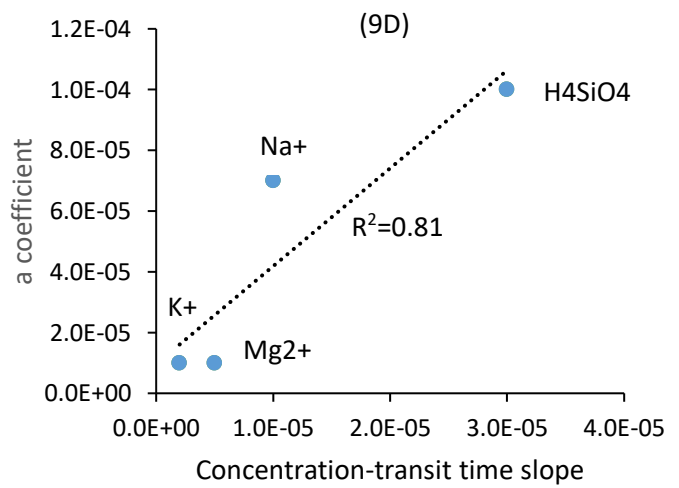
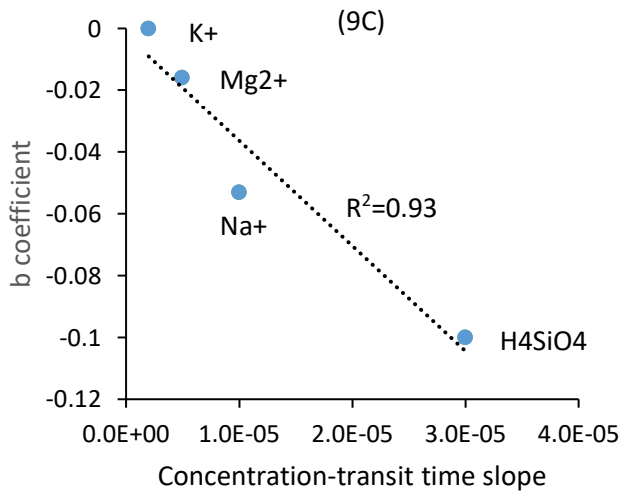
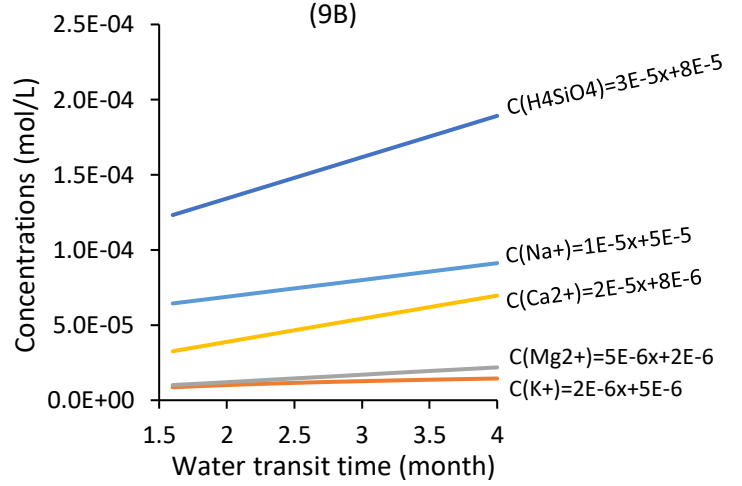
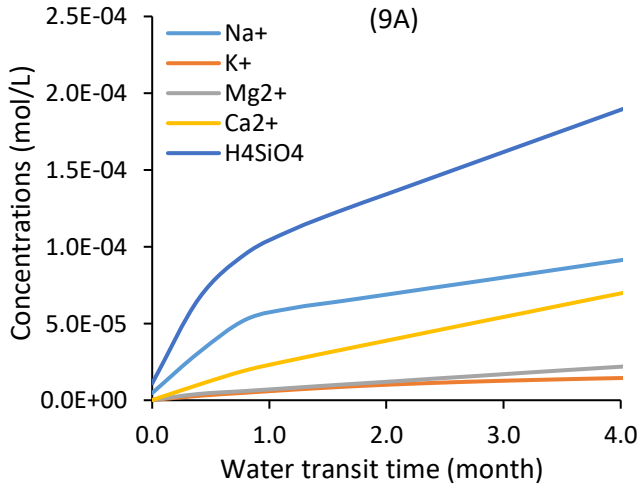


Figure 9

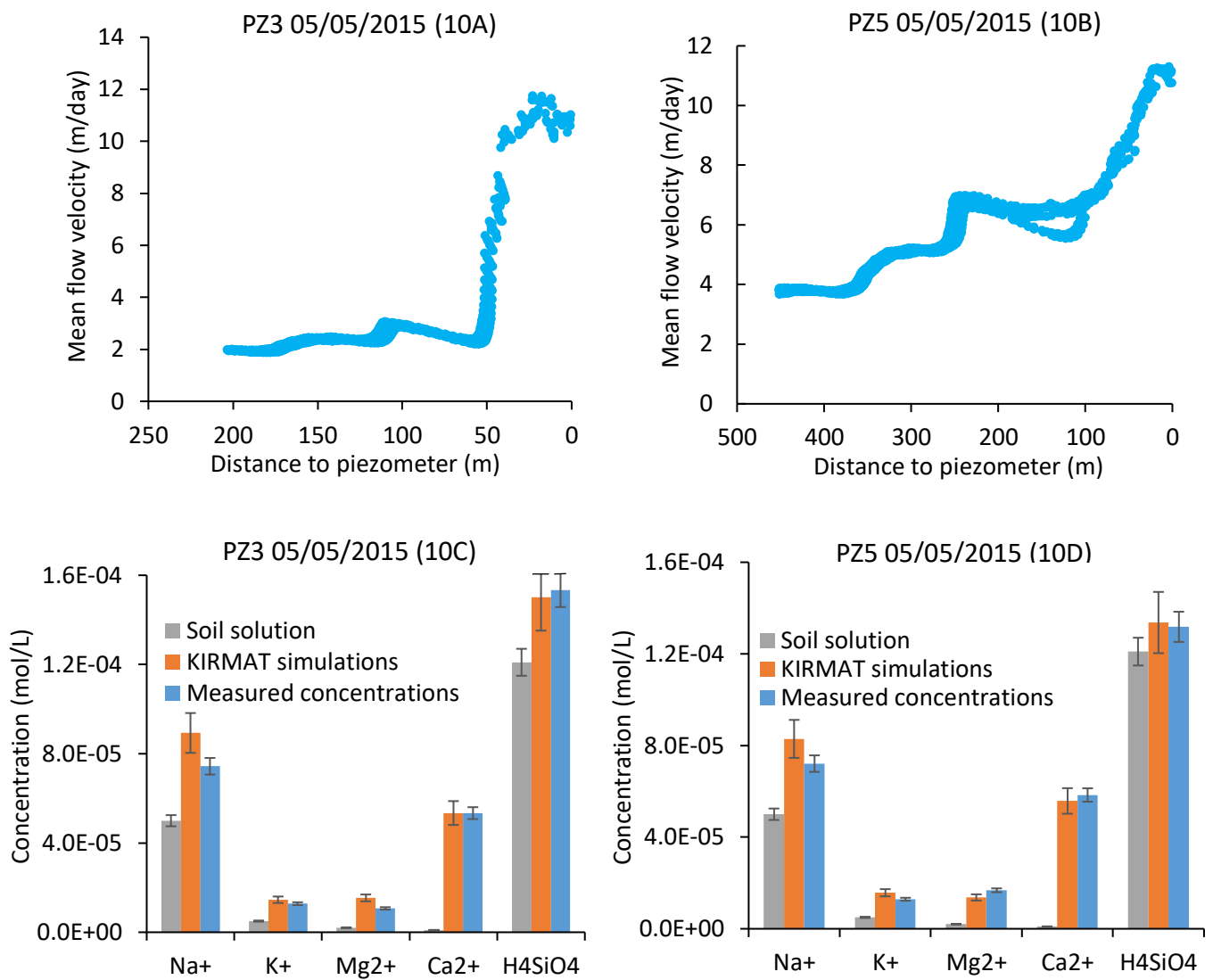


Figure 10

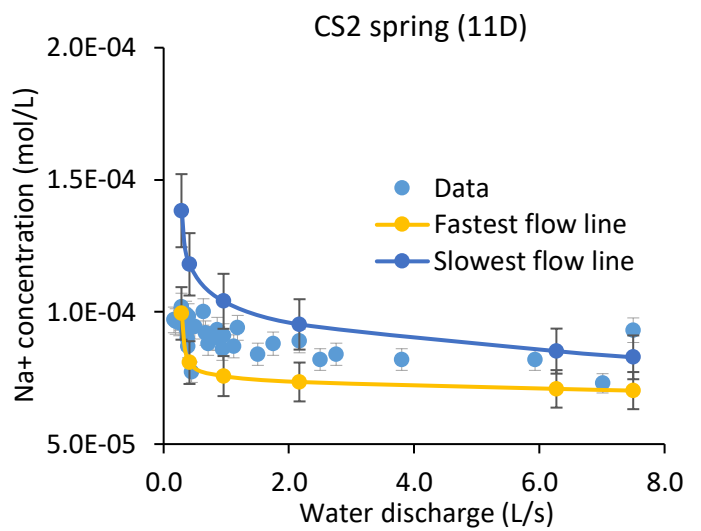
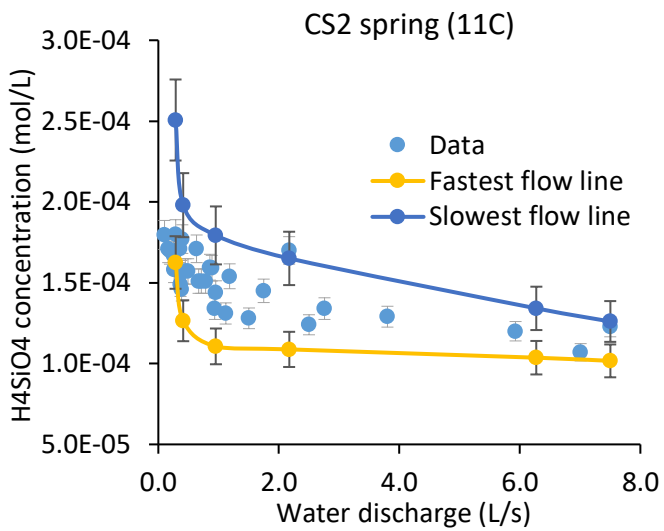
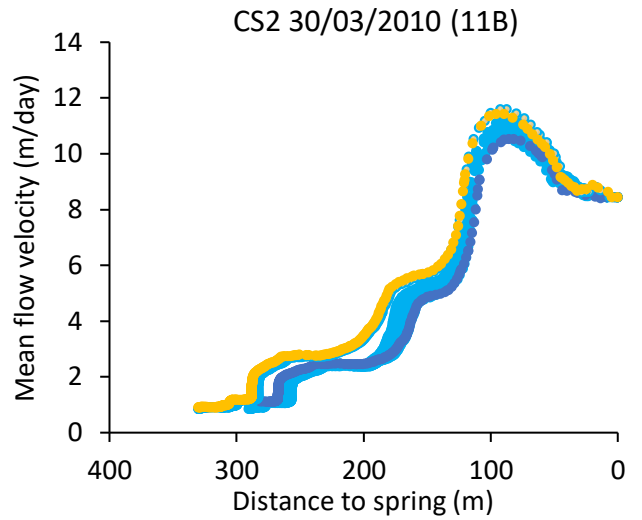
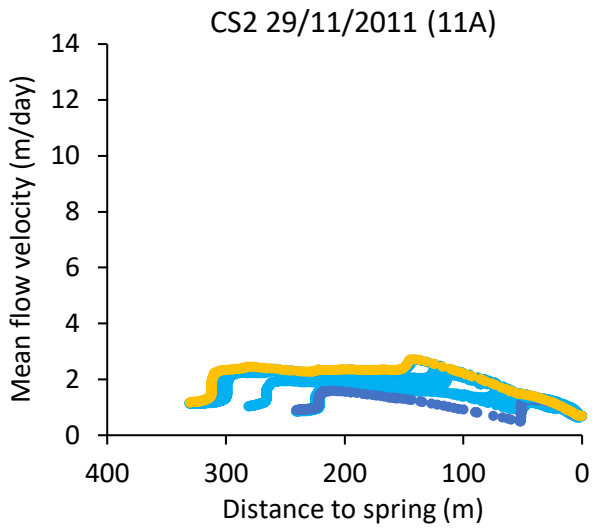


Figure 11

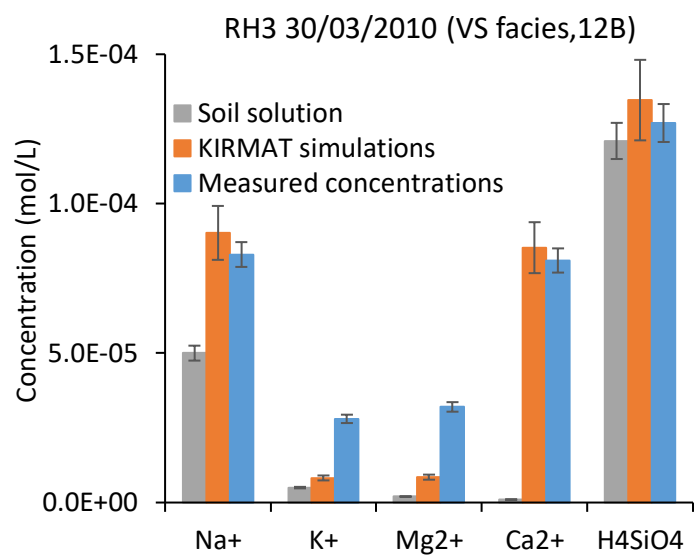
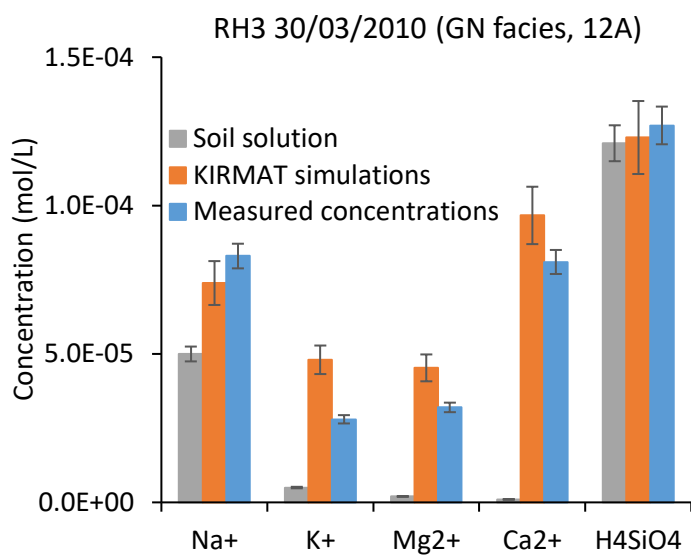


Figure 12

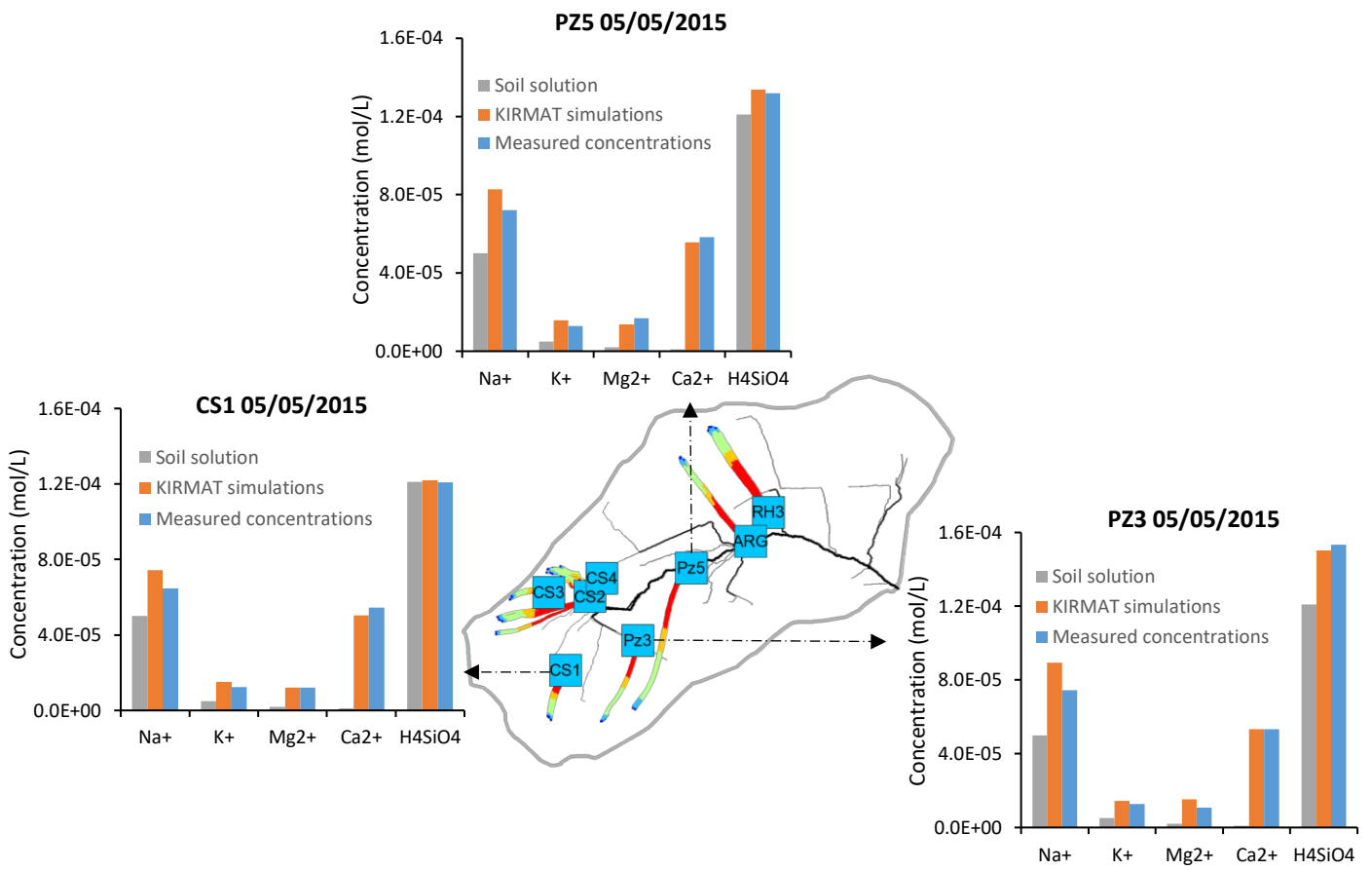


Figure 13